Phase-field crack simulation for thermomechanically coupled problems

by

Zhirou Hu

A thesis
submitted to the University of Ottawa
in partial fulfillment of the
thesis requirement for the degree of
Master of Applied Science
in
Advanced Materials and Manufacturing

Ottawa, Ontario, Canada, 2025

Examining committee

The following served on the Examining Committee for this thesis.

External Examiner: Rong Liu, Professor
Department of Mechanical and Aerospace Engineering
Carleton University

Internal Member: Arnaud Weck, Professor
Department of Mechanical Engineering
University of Ottawa

Supervisor: Tao Jin, Assistant Professor
Department of Mechanical Engineering
University of Ottawa

Declaration of authorship

I hereby certify that this thesis is entirely my own original work except where otherwise indicated. I am aware of the University's regulations concerning plagiarism, including those concerning consequent disciplinary actions. Any use of the works of any other author, in any form, is properly acknowledged at their point of use.

Abstract

In the past several decades, the community of computational solid mechanics has devoted a lot of efforts to develop robust and accurate numerical methods to model fracture initiation and propagation. Some of the prominent methods include the cohesive zone model, the embedded discontinuity approach, and the extended finite element method approach. However, these earlier methods either suffer from pathological mesh-dependence or rely on heuristic fracture tracking algorithm to track crack propagation. These tracking algorithms cannot robustly handle complex crack geometries such as merging and branching even in 2D problems, not to mention complex 3D crack surfaces. Recently, the phase-field method (PFM) has drawn more and more attentions for simulations of crack propagation in solids due to its capability of naturally handling complex crack patterns such as merging and branching. In the view of energy functional, the PFM converts the sharp crack problem into a constrained optimization problem possessing a variational structure. The PFM constructs a nonlinearly coupled problem between the displacement field and the phase-field, which can be solved by either the staggered approach or the monolithic approach. In this thesis, algorithms for both approaches are adopted, which respectively rely on the alternate minimization (AM) and the limited-memory BFGS (L-BFGS) scheme. These two algorithms can both overcome the convergence issues caused by the non-convex nature of the energy functional in fracture mechanics. The PFM algorithms are further combined with heat conduction problems to model the crack propagation under thermomechanically coupled loads. Several numerical examples, including crack simulations in the quenching problem and the thermal barrier coating problem, are provided to demonstrate the capabilities of the developed method. The limitation of current model and possible solutions in future research are discussed.

Acknowledgements

Zhirou Hu is partially supported by the Natural Sciences and Engineering Research Council of Canada (NSERC) under the Discovery Grants Program (funding reference number: RGPIN-2021-02561, principle investigator: Tao Jin, PhD). Their financial support is greatly appreciated.

Dedication

I would like to give my greatest appreciation to Prof. Tao Jin. In the past two years, his guidance for my research helped me get familiar with the advanced research area in mechanics and fostered my logical thinking. The completion of this thesis is impossible without Prof. Jin's academic supports. I am also grateful to my family and friends. Their encouragements helped me overcome many difficulties and challenges in my research. Thanks to all the professors in the Department of Mechanical Engineering at uOttawa. Their excellent lectures provided me with a solid foundation in my research career.

Table of Contents

List of Tables

List of Figures

List of Symbols

A	area
$\boldsymbol{b}$	body force
c	heat capacity
$\mathbb{D}$	degraded material elasticity tensor
d	phase-field value
E	energy
$\boldsymbol{u}$	displacement vector
g	degradation function
$\mathcal{H}$	maximum of positive strain energy in history
$\boldsymbol{J}$	heat flux
l	length scale of phase-field
$\mathbb{P}$	4-th order projection tensor
$\boldsymbol{p}$	surface traction load
q	heat source
T	temperature
T_{ref}	reference temperature
t	time
V	volume
W	work
α	coefficient of thermal expansion
Γ_l	crack surface functional
γ	crack surface density
κ	heat conductivity
λ	first Lamé parameter
μ	second Lamé parameter
Π	total energy functional
ρ	density
$\boldsymbol{\epsilon}$	strain tensor

$\boldsymbol{\epsilon}^+$	positive strain tensor
$\boldsymbol{\epsilon}^-$	negative strain tensor
$\boldsymbol{\sigma}$	stress tensor
$\boldsymbol{\sigma}^+$	positive stress tensor
$\boldsymbol{\sigma}^-$	negative stress tensor
ψ	elastic strain energy density
ψ^+	elastic strain energy density associated with tensile deformation
ψ^-	elastic strain energy density associated with compressive deformation
$\boldsymbol{B}_k$	approximated Hessian matrix at the k-th iteration
$\boldsymbol{H}_k$	inverse of the approximated Hessian matrix at the k-th iteration

Chapter 1

Introduction

In this chapter, the research motivation is firstly introduced. Then, several prominent numerical techniques for crack simulation are briefly introduced, including their strengths and limitations. Lastly, the objectives of this thesis are presented.

1.1 Research motivation

Computational fracture mechanics is an important research topic that is relevant to many real-world engineering applications, such as the hydrogen embrittlement in green energy storage, the hydraulic fracturing in oil and gas industry, the thermal barrier coating system in aerospace engineering, and the structural safety evaluation in civil engineering. In the past several decades, the community of computational solid mechanics devoted a lot of efforts to develop robust and accurate numerical methods to model fracture initiation and propagation. Some of the prominent methods include, for instance, the virtual crack closure technique (VCCT) and the extended finite element method (XFEM). However, these earlier methods either suffer from pathological mesh-dependence or rely on some heuristic fracture tracking algorithms to track crack propagation [5–7]. These tracking algorithms cannot robustly handle complex crack geometries such as merging and branching even in 2D problems, not to mention complex 3D crack surfaces. In the past decade, the phase-field method becomes a popular choice for modeling fracture propagation since it can naturally handle complex crack geometries. This research focuses on addressing several numerical challenges associated with the phase-field crack simulation technique. Several numerical examples are also provided to demonstrate the capability of the phase-field method and its potential for real-world engineering applications.

1.2 Literature review

In this section, the major results of the linear elastic fracture mechanics are summarized. Then, several numerical methods that are commonly applied to model crack propagation are briefly reviewed. Comments are provided regarding the advantages and limitations of each method.

1.2.1 Linear elastic fracture mechanics

Linear elastic fracture mechanics focuses on investigating the stress state near the fracture tip. Generally speaking, the pattern of crack can be classified as three modes [8], namely opening, in-plane shear and out-of-plane shear, for instance, see Fig. 1.1.

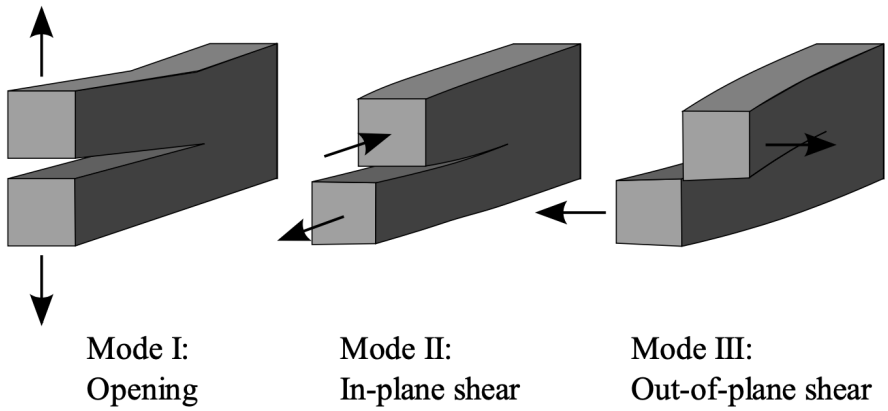

Figure 1.1: Schematic of three basic fracture modes, including the opening mode, the in-plane shear mode, and the out-of-plane shear mode (source: Wikipedia [1]).

The stress around the crack tip has singularity. Based on the linear elastic fracture mechanics, the expression of the crack tip stress has the following general form [9]

$$\sigma_{ij} = \frac{K}{\sqrt{2\pi r}} f_{ij}(\theta), \tag{1.1}$$

where K represents the stress intensity factor (SIF), r is the distance to the crack tip, and θ is the relative angle to the crack plane. Depending on the fracture mode, various stress components have different expressions. For type I fracture (opening mode), which is the

most common fracture mode, the crack tip stress components are

$$\begin{cases} \sigma_x = \frac{K_I}{\sqrt{2\pi r}} \cos\frac{\theta}{2}(1 - \sin\frac{\theta}{2}\sin\frac{3\theta}{2}), \\ \sigma_y = \frac{K_I}{\sqrt{2\pi r}} \cos\frac{\theta}{2}(1 + \sin\frac{\theta}{2}\sin\frac{3\theta}{2}), \\ \tau_{xy} = \frac{K_I}{\sqrt{2\pi r}} \cos\frac{\theta}{2}\sin\frac{\theta}{2}\sin\frac{3\theta}{2}. \end{cases} \tag{1.2}$$

For type II fracture (in-plane shear mode), the crack tip stress components are

$$\begin{cases} \sigma_x = \frac{K_{II}}{\sqrt{2\pi r}} \sin\frac{\theta}{2}(2 + \cos\frac{\theta}{2}\cos\frac{3\theta}{2}), \\ \sigma_y = \frac{K_{II}}{\sqrt{2\pi r}} \sin\frac{\theta}{2}\cos\frac{\theta}{2}\cos\frac{3\theta}{2}, \\ \tau_{xy} = \frac{K_{II}}{\sqrt{2\pi r}} \cos\frac{\theta}{2}(1 - \sin\frac{\theta}{2}\sin\frac{3\theta}{2}). \end{cases} \tag{1.3}$$

For type III fracture (out-of-plane shear mode), the crack tip components are

$$\begin{cases} \tau_{yz} = \frac{K_{III}}{\sqrt{2\pi r}} \cos\frac{\theta}{2}, \\ \tau_{xz} = -\frac{K_{III}}{\sqrt{2\pi r}} \sin\frac{\theta}{2}. \end{cases} \tag{1.4}$$

In the above equations, K_I, K_{II}, and K_{III} are the stress intensity factors corresponding to each fracture mode. Based on these equations, the stress value can be singular (infinite) at the crack tip ($r = 0$), which is obviously unphysical. Consequently, the criterion based on the stress value is not proper to detect fracture initiation and propagation.

In practice, one of the crack propagation criteria is based on the stress intensify factor (SIF). When the SIF value K is greater than the fracture toughness, also known as the critical stress intensify factor (K_c),

$$K > K_c, \tag{1.5}$$

the crack propagates. Alternatively, Griffith [10] and Irwin [11] proposed a criterion of fracture propagation in brittle materials using energy. Based on this criterion, crack propagates when the energy release rate g exceeds the critical value g_c, that is,

$$g > g_c. \tag{1.6}$$

According to the linear elastic fracture mechanics, the critical stress intensity factor (fracture toughness) K_c and the fracture stress σ_f have the following relationship

$$K_c = \sigma_f \sqrt{\pi a} \tag{1.7}$$

where a is crack size. On the other hand, the energy release rate g_c and the critical stress intensity factor K_c have the following relationship

$$g_c = \begin{cases} \dfrac{K_c^2}{E} & \text{plane stress}, \\ \dfrac{(1-\nu^2)K_c^2}{E} & \text{plane strain}, \end{cases} \tag{1.8}$$

where E and ν are the Young's modulus and the Poisson's ratio, respectively. Based on Eqs. (1.7) and (1.8), the critical fracture stress can be expressed as

$$\sigma_f = \begin{cases} \sqrt{\dfrac{g_c E}{\pi a}} & \text{plane stress,} \\ \sqrt{\dfrac{g_c E}{(1-\nu^2)\pi a}} & \text{plane strain.} \end{cases} \tag{1.9}$$

For brittle materials, the above crack propagation criteria are widely adopted. However, in order to model the crack propagation properly, the critical question is how to represent crack, which is a type of spatial discontinuity.

1.2.2 Virtual crack closure technique

The virtual crack closure technique (VCCT) is widely used in fracture mechanics to analyze the growth and behavior of cracks in materials. It is particularly useful for calculating the energy release rate and stress intensity factors in finite element simulations [2]. The hypothesis of the VCCT is that the energy released during crack propagation equals to the energy required to close the same crack. Figure 1.2 illustrates the basic idea of the VCCT. The energy required to close the crack with a length of $a + \Delta a$ is calculated as

$$\Delta E = \frac{1}{2}(X_{1l}\Delta u_{2l} + Z_{1l}\Delta w_{2l}), \tag{1.10}$$

where X, Z are the horizontal and vertical components of the nodal force, Δu_{2l} and Δw_{2l} are the relative displacements in the x- and z-direction on node l. The energy release rate can then be calculated as

$$g = \frac{\Delta E}{\Delta A} = \frac{\Delta E}{h\Delta a}, \tag{1.11}$$

where ΔA is the crack surface area, h is the thickness of the plane, and Δa is the increase of the crack length.

The VCCT can be used to calculate the energy release rate during a finite element simulation. However, the accuracy of the VCCT depends on the mesh refinement near the crack tip. Furthermore, according to the VCCT, the crack is only allowed to propagate along the mesh edges. Therefore, this method works well if the crack path is known *a priori*. When the crack path is unknown beforehand, the numerical result based on the VCCT is inevitably mesh-dependent, therefore, limiting its usage in real-world applications.

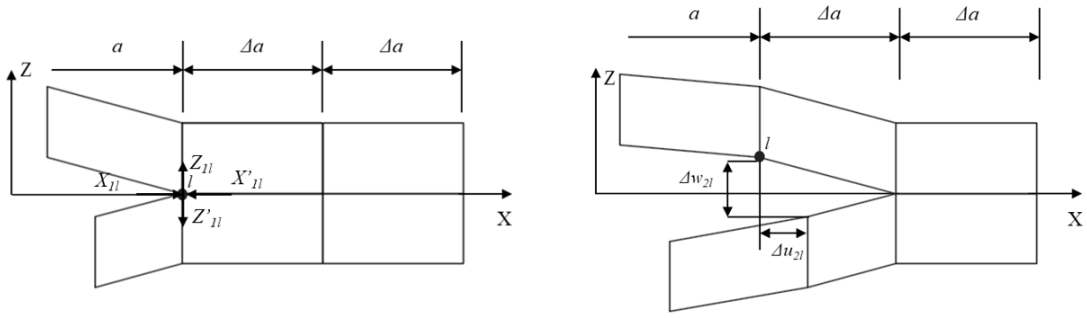

(a) Energy for crack closure

(b) Energy for Crack extension

Figure 1.2: Schematic of the virtual crack closure technique (VCCT), the basic idea of which is that the energy released during crack propagation equals to the energy required to close the same crack [2].

1.2.3 Extended finite element method

In order to address the limitation of the VCCT method, in which the crack is only allowed to propagate along the mesh edges, the extended finite element method (XFEM) [12, 13] is developed to model crack propagation. The most significant advantage of the XFEM is that cracks are allowed to propagate inside an element. This feature is achieved by introducing extra degrees of freedom to represent the discontinuity (crack) inside elements. As a result, the reconstruction of mesh (remeshing) during crack propagation can be avoided [14]. In the XFEM, the standard finite element formulation is enriched by introducing additional discontinuous (shape) interpolation functions. As shown in Fig. 1.3, additional degrees of freedom are introduced on the nodes around the crack path, while the nodes far away from the crack are considered as regular ones [15].

The XFEM has the following features:

- For elements that are far away from crack, the shape functions are the same as the counterparts in standard linear elastic finite element.
- For elements that are fully cut by crack, the enriched shape function is expressed as

$$\psi_J(x) = N_J(x)H(f(x)) \tag{1.12}$$

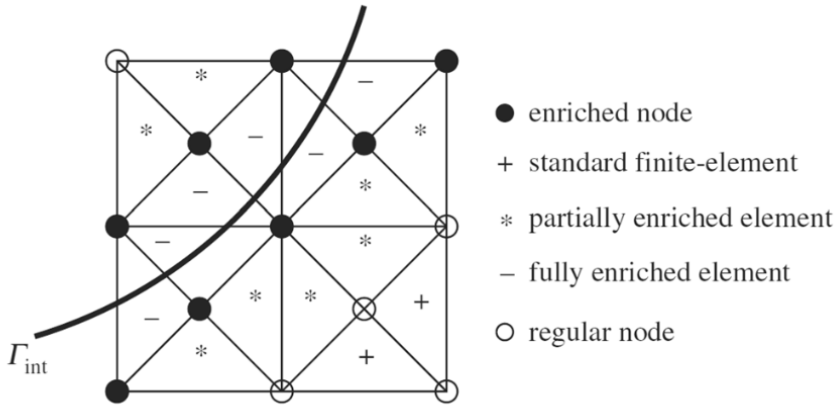

Figure 1.3: Schematic of the extended finite element method (XFEM), which allows crack to propagate inside elements. In this method, the standard finite element formulation is enriched by additional discontinuous (shape) interpolation functions, and additional degrees of freedom are introduced on the nodes around the crack path [3].

where $H(x)$ is the Heaviside function defined as

$$H(x) = \begin{cases} 1 & x \geq 0, \\ -1 & x < 0. \end{cases} \tag{1.13}$$

The level set function [16, 17] is commonly used to describe the location of crack.

$$f(x) = \min_{x \in \Gamma_c} \parallel x - \overline{x} \parallel sign(\boldsymbol{n}^+ \cdot (x - \overline{x})) \tag{1.14}$$

where Γ_c is the crack surface. $\boldsymbol{n}^+$ is normal vector of the crack surface.

- For nodes around crack tip,

$$\psi_K(x) = N_K(x)\boldsymbol{\Phi}(x) \tag{1.15}$$

where

$$\boldsymbol{\Phi}(x) = [\sqrt{r}\sin\frac{\theta}{2}, \sqrt{r}\sin\frac{\theta}{2}\sin\theta, \sqrt{r}\cos\frac{\theta}{2}, \sqrt{r}\cos\frac{\theta}{2}\cos\theta] \tag{1.16}$$

represents the impact of the distance r and the angle θ with respect to the crack tip.

In this way, the displacement can be expressed by the combination of the regular and extended shape functions [18, 19] as

$$\boldsymbol{u^h} = \sum_{I \in S} N_I(x)u_I + \sum_{J \in S_h} N_J(x)H(f(x))a_J + \sum_{K \in S_c} N_K(x) \sum_i \Phi_i(x)b_{Ki} \tag{1.17}$$

where S, S_h and S_c are regular nodes, nodes belonging to elements that are fully cut by crack, and nodes around crack tip, respectively. The extended degrees of freedom are represented by a_J and b_K. With these enriched shape functions, the XFEM can not only represent the discontinuity of crack surface, but also accurately describe the singularity around crack tip.

Despite the aforementioned advantages, the XFEM is mostly used in 2D crack simulations containing simple crack path. This method has limited successes in 3D simulations due to the following reasons. First, when multiple cracks intersect inside a finite element and interact with each other, it is unclear how to construct the enrichment shape functions. Second, for 3D simulations, due to the presence of the enrichment shape functions, it is challenging to perform numerical integration inside an element arbitrarily cut by a crack surface. Third, the XFEM relies on the level-set method to track the crack path, which is not able to handle complex crack patterns such as crack merging and branching.

1.2.4 Cohesive zone model

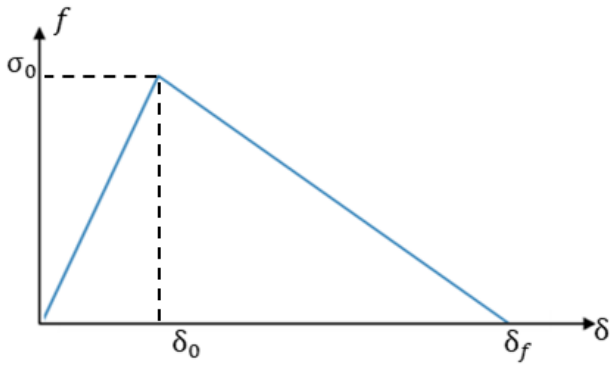

Figure 1.4: Bilinear cohesive relationship: linear stage and damage softening stage

Cohesive zone model (CZM) is introduced to deal with quasi-brittle fracture problems in the plastic zone around crack tips [20]. The CZM assumes that a virtual crack [21, 22] is located in front of the crack tip and there is a pair of traction forces in the relative surfaces of that virtual crack, preventing the crack from propagating. The existence of the traction forces eliminates the singularity of stress in linear elastic fracture mechanics. The traction force value is a function of the opening displacement of the virtual crack δ.

$$f = f(\delta) \tag{1.18}$$

The most common cohesive relationship is bilinear. As shown in Fig. 1.4, at the first stage, the traction force f has a linear increment with the increase of δ, and reaches maximum value when the virtual displacement reaches δ_0. Then, f decreases with the increment of δ due to the damage softening. When δ reaches δ_f, the real crack is formed. Cohesive element [23] is a special element with zero thickness inserted in the possible crack propagation region. Within a cohesive element, the constitutive law is the cohesive relationship shown in Eq. (1.18). The concept of traction force avoids the difficulty encountered by crack tip singularity. However, the cohesive element still requires prediction of crack path, making it challenging to handle complex crack geometries that are unknown beforehand.

1.2.5 Phase-field method

Compared with the virtual crack closure technique (VCCT) and the extended finite element method (XFEM), the phase-field crack simulation does not rely on any heuristic crack tracking strategies. Rather, this method can naturally handle complex crack geometries, and therefore, becomes a popular approach to model crack propagation in many 2D and 3D problems. In literature, there exists a large body of work in the field of phase-field crack formulation, for instance, see [24–35].

The basic idea of the phase-field crack formulation is quite straightforward. Unlike the VCCT or the XFEM method, where sharp crack is directly included in the finite element simulation as shown in Fig. 1.5a, the phase-field method represents the crack in a diffusive manner as shown in Fig. 1.5b. In the phase-field method, a scalar variable d is introduced as the so-called phase-field that represents the damage state of the material. When $d = 0$, it indicates that the material is intact. When $d = 1$, it indicates that the material is fully damaged. The phase-field method assumes that the phase-field variable d continuously changes from 0 to 1. Francfort and Marigo [36] proposed the approach of potential energy minimization to solve the phase-field crack problems in solid mechanics, and several numerical tests are developed to prove the effectiveness of their method [37,38].

Using the phase-field approach to model crack propagation faces at least the following three challenges. First, the total energy functional of the phase-field crack formulation is non-convex. As a result, classical Newton-based approaches encounter convergence difficulties during the nonlinear iterations. In order to address this challenge, various staggered approaches and monolithic approaches are developed, for instance, see [24,29,34]. Second, the phase-field is intrinsically expensive, since highly refined meshes need to be adopted near the crack region. To address this challenge, the adaptive mesh refinement

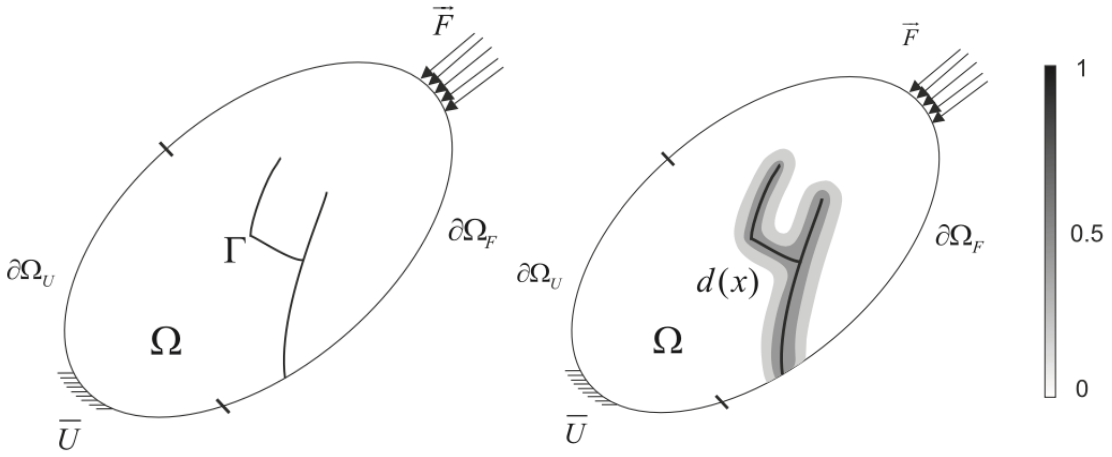

(a) Sharp crack

(b) Diffusive crack

Figure 1.5: Schematic of the phase-field crack formulation, in which the so-called phase-field represents the damage state of the material. When $d = 0$, it indicates that the material is intact. When $d = 1$, it indicates that the material is fully damaged. The phase-field method assumes that the phase-field variable d continuously changes from 0 to 1 [4].

technique is an effective approach, see [27, 34]. Lastly, the crack should not self-heal once it is developed, requiring the phase-field to satisfy the so-called irreversibility condition. The history variable approach based on the maximum strain energy history is a popular choice to enforce this condition due to its simple implementation [24]. Alternatively, other numerical approaches can be adopted, such as the augmented Lagrangian method [29, 39], the active set method [27], the interior-point method [40], and the gradient project method [35].

1.2.6 Thermomechanical interaction

Thermomechanically coupled problem is widely encountered in the area of aerospace, manufacturing, and civil engineering. In this coupled problem, components and structures are under the impact of both mechanical and thermal loading conditions. As a natural phenomenon, thermal expansion is the change of volume in response to temperature change. With applied external constraints or non-uniform distribution of the temperature field, the tendency of the volume change causes stresses inside materials [41]. Generally speaking, thermomechanically coupled problems can be classified into two types:

- Weak coupling: The temperature field significantly influences material deformation

and stress distribution. However, the impact of material deformation on the temperature field is negligible.

- Strong coupling: The temperature field and the material deformation have strong impacts on each other.

Based on the specific type of thermomechanical coupling, the solving technique can either follow the staggered (partitioned) approach or the monolithic approach [42]. The staggered approach is usually used for weak coupling problems, while the monolithic approach is generally used for strong coupling problems.

In many engineering applications, for instance, the thermal barrier coating system, cracks are caused by various thermal effects. Typical examples include quenching cracks [43] caused by thermal shock, which is an instantaneous temperature change results in non-uniform volume change of material, and cracks caused by the mismatch of thermal expansion coefficients [44]. Various approaches, such as the damage mechanics [45], the cohesive zone model [46], and the XFEM [47], are adopted to model thermal-induced cracks.

1.3 Research objectives

This thesis aims to accomplish the following tasks:

- The phase-field approach will be combined with an adaptive mesh refinement technique to represent preexisting cracks that possess complex patterns. The phase-field approach is intrinsically expensive since highly refined meshes need to be adopted to resolve the characteristic length-scale. The adaptive mesh refinement can significantly reduce the computational cost by only refining meshes near the crack region.

- Several numerical techniques will be developed to overcome the convergence difficulties inside the nonlinear iterations. The total energy functional of the phase-field crack formulation is non-convex. As a result, the classical Newton-Raphson method encounters convergence issues during the nonlinear iterations. In order to overcome this difficulty, the staggered approach based on the alternate minimization and the monolithic approach based on the limited-memory BFGS method will be presented, which can significantly improve the robustness of the phase-field simulation.

- A computational framework will be developed to model crack propagation driven by thermal effects. The heat conduction equation will be integrated into the phase-field

crack formulation. As a result, the coupled problem involves the temperature field, the displacement field, and the phase-field. Several solving strategies are presented to effectively solve the coupled problem.

- Multiple numerical examples will be provided to demonstrate the capabilities of the developed numerical approaches in modeling crack propagation under various mechanical and thermal loading conditions. In particular, the crack propagation in a thermal barrier coating system will be investigated for real-world engineering applications.

- All the presented numerical methods and algorithms will be implemented in deal.II [48], which is an open-source C++ finite element library. All the source codes and input files used in this thesis can be found on GitHub[1] to support open science and reproducible research.

The original contributions of this thesis include:

- Extend the limited-memory BFGS (L-BFGS) method, originally proposed by Prof. Tao Jin's group [34], from the mechanical phase-field problem to the thermomechanically coupled phase-field problem.

- Demonstrate the equivalence of the staggered approach and the L-BFGS monolithic approach in the phase-field formulation. Moreover, the latter requires fewer iterations to achieve convergence during the nonlinear solving process.

- Implement the computational framework in the deal.II library [48], which can be extended to solve more complex problems in the future.

The remaining part of the thesis is organized as follows. In Chapter 2, the phase-field method is introduced to represent preexisting crack in a diffusive manner. Moreover, an adaptive mesh refinement technique is combined with the phase-field method to reduce the computational cost. In Chapter 3, the variational structure, which is the theoretical foundation of the phase-field crack formulation, is firstly introduced. Then, the derivation of the weak form and the finite element discretization are presented. Several numerical strategies are developed to overcome the convergence difficulties during the nonlinear iterations caused by the non-convexity of the energy functional. Lastly, the phase-field crack formulation is further extended to consider the thermal effect on the crack propagation modeling. In Chapter 4, multiple numerical examples are provided to demonstrate the

[1] https://github.com/taojinllnl/

capabilities of the developed numerical methods in modeling crack propagation under various mechanical and thermal loading conditions. The results and convergence performance of the presented solving strategies are also compared. In Chapter 5, the conclusions of the thesis are summarized, and several avenues are discussed to further improve the phase-field crack modeling.

Chapter 2

Phase-field representation of crack

In this chapter, the theory and numerical implementations of the phase-field method [24, 25] are reviewed in detail to model sharp cracks in a diffusive manner. First, a simple one-dimensional scenario is provided to illustrate the basic idea of the phase-field method for crack representation. Then, a variational approach is formulated to derive the strong form of the phase-field method. Based on this strong form, the corresponding weak form and the finite element formulation are obtained. The phase-field crack formulation is intrinsically expensive, since a highly refined mesh needs to be applied to the region around the crack path. Using the same high mesh resolution in the whole computational domain is prohibitively expensive, particularly for three-dimensional problems, Therefore, adaptive mesh refinement (AMR) techniques are indispensable for any practical phase-field simulations. An AMR technique based on the so-called Kelly error estimator [49] is provided. To illustrate the phase-field crack modeling with the adaptive mesh refinement, several two-dimensional and three-dimensional numerical examples are provided to represent preexisting sharp cracks in a diffusive manner.

2.1 Phase-field representation of crack topology

This section starts with a simple one-dimensional example to illustrate the basic idea of using the phase-field method to represent the sharp crack topology. Then, a variational approach is used to derive the strong form of the phase-field formulation, Subsequently, the weak form and the finite element formulation are provided.

2.1.1 One-dimensional scenario

Crack can be considered as a type of discontinuity in the displacement field, which in general is challenging to deal with during finite element simulations. The basic idea of the phase-field method for crack modeling is to represent the sharp crack topology (discontinuity) in a diffusive manner. Consider an one-dimension scenario shown in Fig. 2.1a, where a crack of the bar exists at the location of $x = 0$. This sharp crack can be represented by a scalar field variable $d(x) \in [0, 1]$, where $d = 0$ represents the intact (undamaged) state and $d = 1$ represents the crack (fully damaged) state. This scalar field variable $d(x)$ is called *the phase-field*. Obviously, the distribution of the phase-field is discontinuous,

$$\begin{cases} d = 1 & \text{for } x = 0, \\ d = 0 & \text{for } x \neq 0. \end{cases} \tag{2.1}$$

In order to avoid the numerical difficulties associated with the discontinuity, an alternative approach to represent the crack topology is to adopt the following exponential function as an approximation,

$$d = e^{-|x|/l}, \tag{2.2}$$

where l is a length-scale parameter. Essentially, this exponential function smears out the sharp crack $d = 1$ along the length-scale l, as shown in Fig. 2.1b. As the length-scale parameter l goes to zero, the sharp crack topology can be recovered.

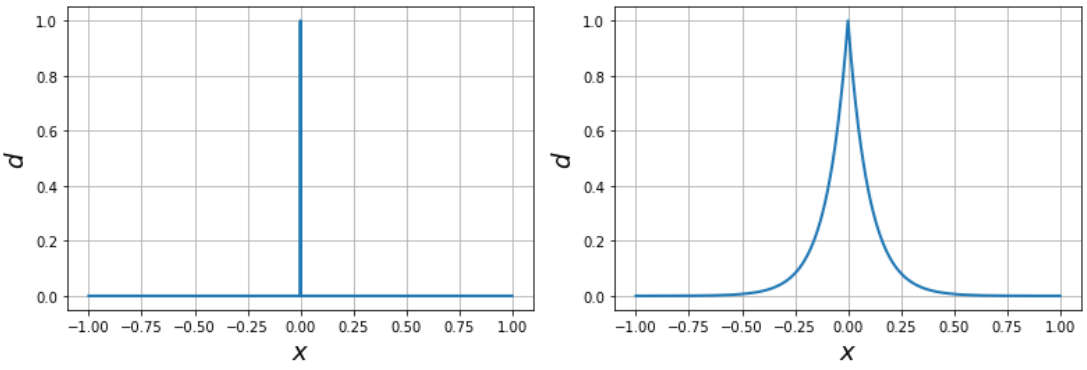

(a) Sharp crack topology

(b) Diffusive crack representation

Figure 2.1: 1D phase-field Function: Replacing the sharp crack, phase-field makes diffusive crack continuous in the computational domain

2.1.2 Variational approach

The above simple one dimensional case can be extended to a more general setup [24]. The crack density function per volume is defined as

$$\gamma(d,\, \nabla d) = \frac{1}{2l} d^2 + \frac{l}{2} \nabla d \cdot \nabla d. \tag{2.3}$$

Therefore, the regularized crack functional is expressed as

$$\Gamma_l(d) = \int_\Omega \gamma(d,\, \nabla d) \mathrm{d}V = \frac{1}{2l} \int_\Omega (d^2 + l^2 \nabla d \cdot \nabla d)\, \mathrm{d}V. \tag{2.4}$$

Assume that the critical energy release rate of the solid is g_c, then the crack energy can be written as

$$\Pi_{\text{crack}}(d) = g_c \Gamma_l(d) = g_c \int_\Omega \gamma(d,\, \nabla d) \mathrm{d}V = \frac{g_c}{2l} \int_\Omega (d^2 + l^2 \nabla d \cdot \nabla d)\, \mathrm{d}V. \tag{2.5}$$

The phase-field function $d(\boldsymbol{x})$ can be decided by minimizing the crack energy functional, that is,

$$d(\boldsymbol{x}) = \underset{d \in W_\Gamma}{\arg\min} \left\{ \Gamma_l(d) \right\} \tag{2.6}$$

subject to the boundary condition

$$W_\Gamma = \left\{ d(\boldsymbol{x}) | d(\boldsymbol{x}) = 1.0,\, \forall \boldsymbol{x} \in \Gamma \right\},$$

where Γ represents the sharp crack.

For the regularized crack functional shown in Eq. (2.4), the first variation can be expressed as the following directional derivative

$$\begin{aligned} D_{\delta d} \Gamma_l(d) &= \left. \frac{d}{d\epsilon} \right|_{\epsilon=0} \Gamma_l(d + \epsilon \delta d) \\ &= \left. \frac{d}{d\epsilon} \right|_{\epsilon=0} \frac{1}{2l} \int_\Omega \left[(d + \epsilon \delta d)^2 + l^2 \nabla (d + \epsilon \delta d) \cdot \nabla (d + \epsilon \delta d) \right] \mathrm{d}\Omega \\ &= \frac{1}{l} \int_\Omega \left[d \delta d + l^2 (\nabla d) \cdot (\nabla \delta d) \right] \mathrm{d}\Omega = 0. \end{aligned}$$

Based on the above first variation, using the techniques of integration by part and the divergence theorem,

$$\frac{1}{l} \int_\Omega (d - l^2 \Delta d) \delta d \, \mathrm{d}\Omega + l \int_{\partial\Omega} (\nabla d \cdot \boldsymbol{n}) \delta d \, \mathrm{d}A = 0.$$

Therefore, the strong form, or the governing partial differential equation, and the boundary conditions can be obtained as [24, 25]

$$\begin{cases} d - l^2 \Delta d = 0 & \text{in } \Omega, \\ \nabla d \cdot \boldsymbol{n} = 0 & \text{on } \partial\Omega, \end{cases} \tag{2.7}$$

where $\Delta(\bullet)$ is the Laplace operator. The corresponding weak form is obtained as

$$\int_\Omega \left[d\delta d + l^2 (\nabla d) \cdot (\nabla \delta d) \right] \, \mathrm{d}\Omega = 0.$$

After the domain Ω is discretized by a finite element mesh, assume that at node A the corresponding test function is $\delta d_A(\boldsymbol{x}) = N_A(\boldsymbol{x})$, and the phase-field solution can be expressed as

$$d(\boldsymbol{x}) = N_B(\boldsymbol{x}) d_B,$$

where d_B is the phase-field nodal solution and the Einstein summation is used. Then, the following linear system can be formed as

$$\mathbf{K}\boldsymbol{d} = \mathbf{0}, \tag{2.8}$$

where the component of the stiffness matrix $\mathbf{K}$ is

$$K_{AB} = \int_\Omega \left[N_A N_B + l^2 (\nabla N_A) \cdot (\nabla N_B) \right] \, \mathrm{d}\Omega = (N_A, N_B) + (l^2 \nabla N_A, \nabla N_B).$$

In the above equation, $(\bullet, \bullet)$ is the standard bilinear operator, and the solution vector $\boldsymbol{d}$ is composed of the phase-field value at individual finite element node.

2.2 Adaptive mesh refinement

As discussed above, the diffusive representation of the crack converges to the sharp crack topology when the phase-field length-scale l goes to zero. In practice, it is important to use a small value of l, and the mesh size h inside the crack region needs to be smaller than the length-scale l. Therefore, the phase-field representation of crack is intrinsically expensive. For any practical simulations, particularly three-dimensional simulations, it is prohibitively expensive to use the same fine mesh resolution in the entire computational domain. Therefore, the adaptive mesh refinement technique becomes necessary.

The idea of the adaptive mesh refinement is to only refine regions of interest, in this case, the crack region. In this work, the methodology of *solve-estimate-mark-refine*

paradigm is adopted. The "solve" stage means to solve the finite element problem, for instance, as shown in Eq. (2.8). Once the solution vector is obtained from the "solve" stage, the "estimate" stage is to estimate the error inside each element based on some criterion. Then, the "mark" stage is to mark those elements that have large errors for refinement and those that have small errors for coarsening. Finally, the "refine" stage executes the mesh refinement and coarsening. From the above process, it can be seen that a good error estimator is key to a successful adaptive mesh refinement technique. In this work, the so-called Kelly error estimator [49] is adopted. The error estimation of element K is expressed as

$$\eta_K^2 = \sum_{F \in \partial\Omega^{(K)}} c_F \int_{\partial\Omega^{(K)}} \left[\left[a \frac{\partial u_h}{\partial n} \right]\right]^2 \mathrm{d}A, \tag{2.9}$$

where $[[\bullet]]$ represents the jump of the quantity at the element interface, and $a\frac{\partial u_h}{\partial n}$ is the solution gradient along the normal direction at the element interface.

During the "estimate" stage, the error η_K is calculated for each element. During the "mark" stage, all the elements can be ranked according to their error η_K from high to low. The top 30% elements, for example, are labeled for refinement, while the bottom 30% elements, for instance, are labeled for coarsening. Then, in the "refine" stage, the refinement and the coarsening are executed.

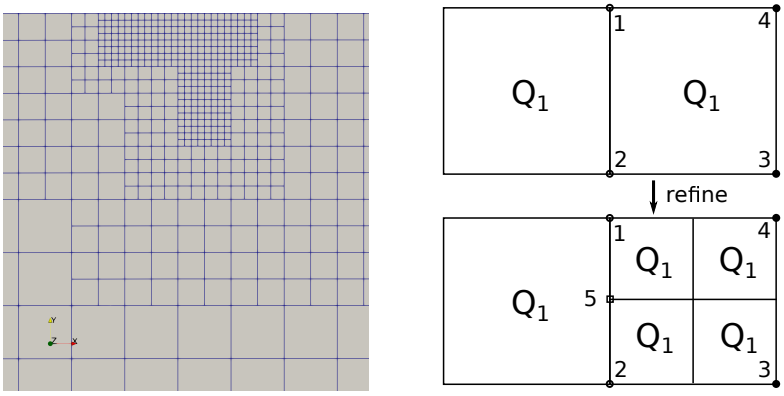

(a) Adaptively refined mesh (b) Hanging nodes

Figure 2.2: During (a) the adaptive mesh refinement, (b) hanging nodes are generated at the edges/faces shared by elements of different refinement level. These hanging nodes, along with the nodes that are prescribed with essential boundary conditions, are treated as constrained nodes.

In the context of the finite element method with adaptive mesh refinement, Fig. 2.2a shows an example of an adaptively refined mesh, and Fig. 2.2b shows the hanging nodes

at the edges/faces shared by elements of different refinement level during mesh refinement. The degrees of freedom associated with the hanging nodes and the nodes that are prescribed with essential boundary conditions are treated as algebraic constraints in the assembled linear system. For instance, in Fig. 2.2b, the right element is refined by one more level than the left element, resulting in a hanging node (node 5) at the interface. Assume that both elements before the refinement use the bilinear shape functions (Q1). Then, the degrees of freedom (DoF) of x_5 associated with the hanging node (node 5) can be expressed by the DoFs of x_1 and x_2 associated with the neighboring nodes (nodes 1 and 2) in the following linear relationship,

$$x_5 = \frac{1}{2}x_1 + \frac{1}{2}x_2.$$

Moreover, if node 4 is prescribed with an essential boundary condition, then the DoF of x_4 associated with this node can be written as

$$x_4 = k_4,$$

where k_4 represents the prescribed value. In general, the DoF of a constrained node can be expressed in the following linear relationship

$$x_i = c_{ij}x_j + k_i,$$

where c_{ij} represents the coefficients due to the hanging-node constraints and k_i represents inhomogeneous constraints such as the essential boundary conditions. The entire constraints can be written in a linear system as below:

$$\boldsymbol{x} = \mathbf{C}\boldsymbol{x} + \boldsymbol{k}.$$

Particularly, the coefficient matrix $\mathbf{C}$ is idempotent, meaning that $\mathbf{C}^2 = \mathbf{C}$. For a linear system $\mathbf{A}\boldsymbol{x} = \boldsymbol{b}$ with the above set of constraints, the following modified linear system [50] can be solved instead

$$\left(\mathbf{C}^{\mathrm{T}}\mathbf{A}\mathbf{C} + \mathbf{I}_{d_c}\right)\hat{\boldsymbol{x}} = \mathbf{C}^{\mathrm{T}}\left(\boldsymbol{b} - \mathbf{A}\boldsymbol{k}\right) \tag{2.10}$$

and then, the true solution $\boldsymbol{x}$ can be recovered as

$$\boldsymbol{x} = \mathbf{C}\hat{\boldsymbol{x}} + \boldsymbol{k}. \tag{2.11}$$

In the modified linear system, the matrix $\mathbf{I}_{d_c}$ is defined as

$$(\mathbf{I}_{d_c})_{ij} = \begin{cases} 0 & \text{if} \quad i \neq j, \\ 1 & \text{if} \quad i = j \in \mathcal{T}, \\ 0 & \text{if} \quad i = j \notin \mathcal{T}, \end{cases}$$

where $\mathcal{T}$ represents the set of the DoFs of the constrained nodes, including the hanging nodes and the nodes prescribed with essential boundary conditions. Obviously, for a linear system without any nodal constraints, we have $\mathbf{C} = \mathbf{I}$, $\mathbf{I}_{d_c} = \mathbf{0}$, and $\boldsymbol{k} = \mathbf{0}$.

2.3 Numerical examples for crack topology representation

In this section, several two-dimensional (2D) and three-dimensional (3D) numerical examples are provided to demonstrate the phase-field representation of the crack topology. In all the numerical examples, the phase-field length-scale is chosen as $l = 0.005$ mm, and the finite element mesh is adaptively refined multiple times based on the phase-field solution obtained by solving the linear system given in Eq. (2.8).

2.3.1 Single crack in 2D

In the first example, a single preexisting crack is located in the center of the unit square computational domain. The Dirichlet boundary condition is set such that at the sharp crack the phase-field value is $d = 1.0$. The initial coarse finite element mesh is consecutively refined based on the solve-estimate-mark-refine paradigm. Figure 2.3 illustrate the phase-field distribution obtained from various numbers of adaptive mesh refinement. As the number of adaptive refinement increases, the phase-field provides a more and more accurate representation of the original sharp crack topology. Due to the adaptive mesh refinement, instead of the global mesh refinement, only the mesh around the sharp crack region is refined. Therefore, the computational cost does not increase significantly during the adaptive mesh refinement.

2.3.2 Intersecting cracks in 2D

In the second example, two preexisting cracks intersect with each other inside the unit square computational domain. Similarly, the Dirichlet boundary condition is set such that at the two sharp cracks the phase-field value is set as $d = 1.0$. Figure 2.4 show the phase-field distribution that represents the two intersecting cracks. As the number of adaptive mesh refinement increases, the phase-field provides a more and more accurate representation of the original sharp crack topology. Similar as before, only regions near the crack region need to be refined, which is the advantage of the adaptive mesh refinement technique.

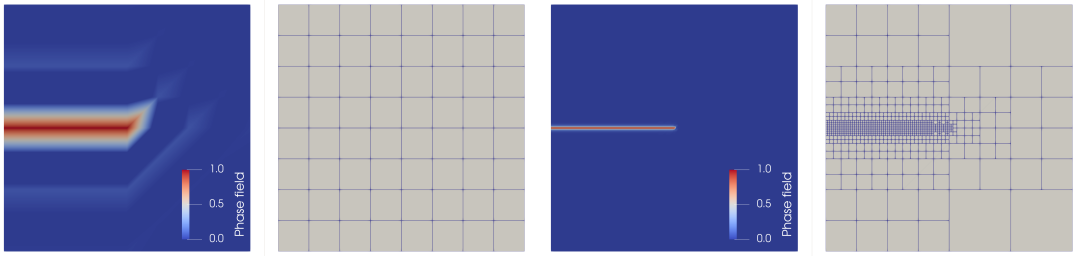

(a) Original coarse mesh

(b) Adaptively refined 4 times

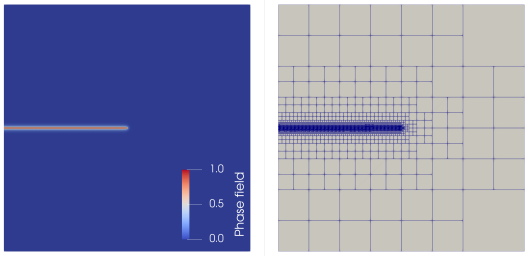

(c) Adaptively refined 9 times

Figure 2.3: Single crack in 2D. A single preexisting crack inside the unit square computational domain is represented by the phase-field $d(\boldsymbol{x})$. The quality of the solution improves as the number of the adaptive mesh refinement increases.

2.3.3 Single crack in 3D

As the last numerical example in this chapter, a single preexisting crack inside a 3D solid is represented by the phase-field. Generally, 3D finite element simulations are intrinsically expensive since the number of degrees of freedom increases in a cubic fashion during mesh refinement. Therefore, the adaptive refinement technique is indispensable for 3D phase-field crack modeling to control the increase of the computational cost. As shown in Fig. 2.5, the phase-field approach can also straightforwardly represent the sharp crack topology inside 3D solids.

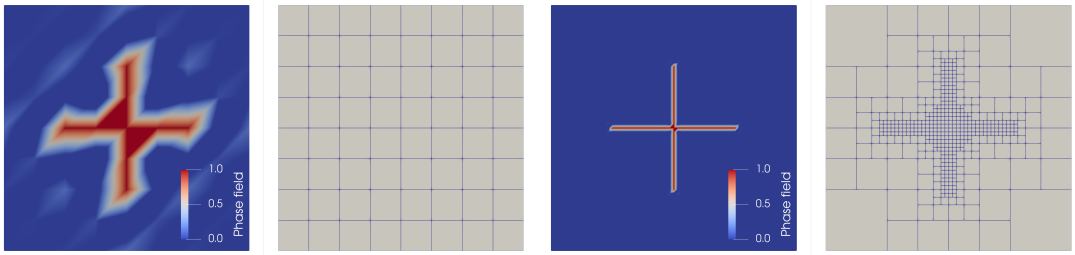

(a) Original coarse mesh

(b) Adaptively refined 4 times

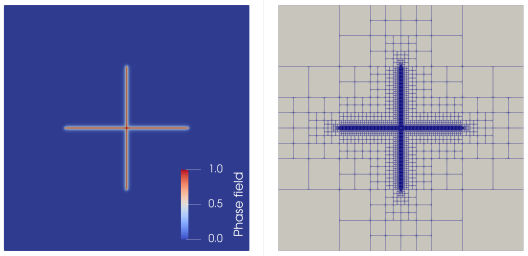

(c) Adaptively refined 9 times

Figure 2.4: Intersecting 2D cracks. Two preexisting cracks intersect with each other in the unit square computational domain. The phase-field method can easily represent the topology of the intersecting sharp cracks.

2.4 Summary

Representing complex crack geometry is challenging in finite element simulations. The phase-field method provides an effective framework to represent the sharp crack topology in a diffusive manner. The phase-field method solves a Laplace-type boundary value problem, which is straightforward to implement. Furthermore, the adaptive mesh refinement technique is introduced to confine the high mesh resolution refinement only to the crack region, which is crucial to reduce the computational cost. This chapter only focused on presenting the phase-field method and the corresponding numerical implementations to represent preexisting cracks. The cracks themselves, however, do not develop or propagate. In the next chapter, the phase-field crack modeling will be further combined with the balances of linear and angular momentum equations, in which the crack will evolve and propagate under mechanical loading conditions.

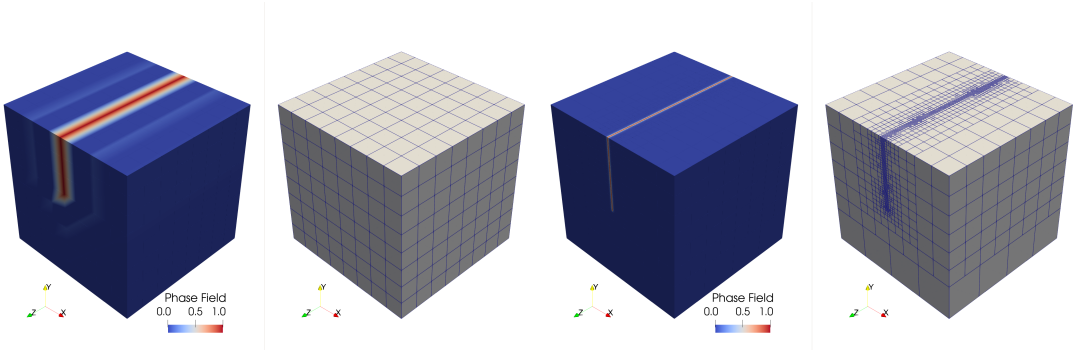

(a) Original coarse mesh

(b) Adaptively refined 4 times

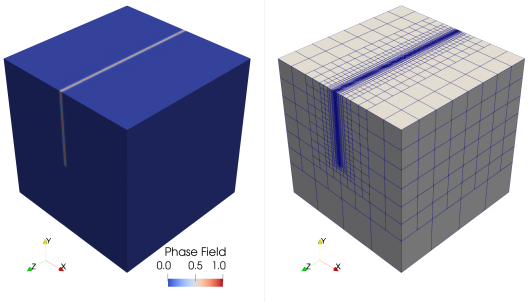

(c) Adaptively refined 7 times

Figure 2.5: Single 3D crack. The phase-field can also represent sharp crack in three-dimensional problems, and the adaptive mesh refinement is crucial to control the computational cost.

Chapter 3

Phase-field model of crack propagation

In this chapter, the phase-field method is developed to model crack propagation due to mechanical and thermal loads. First, the total energy functional considering the energy dissipation associated with the crack propagation is introduced. Then, the variational method is applied to obtain the Euler-Lagrange equations that govern the crack propagation process. Since the total energy functional involves both the displacement field and the phase-field, the crack propagation can be treated as a coupled problem. Due to the non-convexity of the total energy functional, the classical Newton-Raphson iterations typically encounter convergence difficulties. Therefore, the phase-field crack problem can be solved by either a monolithic approach [51] that simultaneously solves for the displacement field and the phase-field, or a staggered approach [24] that solves for the displacement field and the phase-field alternately. The above algorithms are further combined with a heat conduction equation to model the crack propagation under thermal loads.

3.1 Energy principle

In this section, the total energy functional for the crack propagation is introduced. Based on this energy functional, the phase-field crack propagation problem is expressed as a minimization problem. In order to prevent crack from self-healing, the history variable approach is adopted [24]. Then, the corresponding Euler-Lagrange equations are derived.

3.1.1 Total energy functional

The minimum potential energy principle is the foundation of the finite element method in solid mechanics. For a linear elastic problem without any damage involved, the total energy functional of an intact material Π can be written as

$$\Pi = U + V$$

where U and V are the strain energy stored in the deformed material and the work associated with external forces applied to the material, respectively. However, when fracture is introduced, the total potential energy must include the dissipation term since the formation of crack surface dissipates energy. As discussed in [36], the total potential energy of a material sample containing cracks is expressed as

$$\Pi = E + E_d - W_{ext} \tag{3.1}$$

where E, E_d, and W_{ext} are the strain energy degraded due to damage, the dissipation energy due to crack propagation, and external work respectively. Let $\boldsymbol{u}(\boldsymbol{x})$ represent the unknown displacement field vector and $d(\boldsymbol{x})$ represent the unknown phase-field scalar. The energy functional of the fractured solid system is expressed as

$$\Pi(\boldsymbol{u}, d) = \int_\Omega \psi(\boldsymbol{\varepsilon}(\boldsymbol{u}), d)\, dV + \int_\Omega g_c \gamma(d, \nabla d)\, dV - \int_\Omega \boldsymbol{b} \cdot \boldsymbol{u}\, dV - \int_{\partial\Omega} \boldsymbol{p} \cdot \boldsymbol{u}\, dA, \tag{3.2}$$

where $\boldsymbol{b}$ is the body force, $\boldsymbol{p}$ is the traction load, $\boldsymbol{\epsilon} = \nabla^{(s)}\boldsymbol{u}$ is the small deformation linear strain tensor, ψ represents the strain energy density function, g_c is the critical energy release rate, and Γ_l is an approximation of the crack surface area. Particularly, the approximated crack surface Γ_l is defined as

$$\Gamma_l(d) = \int_\Omega \gamma(d, \nabla d) \mathrm{d}\Omega = \int_\Omega \frac{1}{2l} \left(d^2 + l^2 \nabla d \cdot \nabla d\right) \mathrm{d}\Omega, \tag{3.3}$$

where $\gamma(d, \nabla d)$ is considered as the crack surface density function, and l is the phase-field length-scale parameter.

3.1.2 Minimization

The total energy functional depends on both the phase-field $d(\boldsymbol{x})$ and the displacement field $\boldsymbol{u}(\boldsymbol{x})$. When crack propagates, the distribution of the crack always minimizes the total energy functional Π. Firstly addressed by Francfort and Marigo [36,37], the fracture

problem is converted into an optimization problem. The displacement field and the phase-field can be solved by minimizing the total energy functional

$$(\boldsymbol{u}, d) = arg \min_{u,d \in W_{u,\Gamma}} \{\Pi(\boldsymbol{u}, d)\} \tag{3.4}$$

where $W_{u,\Gamma}$ is a set of boundary conditions for the arguments. Following this approach, the crack propagation problem is expressed as the above minimization problem.

3.1.3 Degradation function

When damage is involved, the energy stored in materials is dissipated. Therefore, a degradation function needs to be introduced to represent the effect of damage. During crack propagation, it is assumed that the elastic strain energy is only degraded due to the tensile effect while the compression has no contribution to fracture [24]. Based on this assumption, the degradation function is only applied to the tensile part of the strain energy. Thus, the strain energy density is modified as [24, 25]

$$\psi(\varepsilon, d) = g(d)\psi^{+}(\boldsymbol{\varepsilon}) + \psi^{-}(\boldsymbol{\varepsilon}), \tag{3.5}$$

where $g(d)$ is a degradation function, ψ^{+} is the strain energy associated with the tensile effect, and ψ^{-} is the strain energy associated with compression.

The phase-field $d(\boldsymbol{x})$ indicates the damage in the material, which causes the degradation of the stored elastic energy. As a result, a degradation function needs to be introduced. The degradation function should satisfy following properties

$$\begin{cases} g(0) = 1, \\ g(1) = 0, \\ g'(1) = 0, \\ g'(d) < 0. \end{cases}$$

The physical meanings of these equations are:

- in an intact material, $d = 0$, the energy stored in material has no degradation;
- in a fully damaged material, $d = 1$, the stored elastic energy is reduced to 0;
- in a fully damaged material, the phase-field can no longer evolve;
- when damage increases, the remaining elastic energy decreases.

The degradation function adopted in this work is expressed as the following quadratic form [24, 25]

$$g(d) = (1-d)^2. \tag{3.6}$$

Notice that Eq. (3.6) is only one of the possible degradation functions. There are many other functions satisfying the above features. For example, the cohesive zone hypothesis might be combined with the phase-field model [28], resulting in new forms of degradation function.

3.1.4 Strain energy decomposition

In order to consider the different effects between the tension and compression on the strain energy degradation, the strain tensor is decomposed as the tensile and the compression parts [24, 25]

$$\boldsymbol{\varepsilon} = \boldsymbol{\varepsilon}^+ + \boldsymbol{\varepsilon}^- \tag{3.7}$$

The positive and negative strain tensors are defined as

$$\boldsymbol{\varepsilon}^{\pm} = \sum_{\alpha} \langle \varepsilon_\alpha \rangle^{\pm} \boldsymbol{M}_\alpha, \tag{3.8}$$

where

$$\boldsymbol{M}_\alpha = \boldsymbol{n}_\alpha \otimes \boldsymbol{n}_\alpha$$

and the bracket operators $\langle \cdot \rangle$ are defined as

$$\langle x \rangle_{\pm} = \frac{x \pm |x|}{2}.$$

In the above equation, ϵ_α and $\boldsymbol{n}_\alpha$ represent a pair of eigenvalue and eigenvector of the strain tensor $\boldsymbol{\varepsilon}$. The derivatives of the positive and negative strain tensors $\boldsymbol{\varepsilon}^+$ and $\boldsymbol{\varepsilon}^-$ define the following two projection tensors [24]

$$\mathbb{P}^{\pm} := \frac{\partial \boldsymbol{\varepsilon}^{\pm}}{\partial \boldsymbol{\varepsilon}} \tag{3.9}$$

Let $H(x)$ represent the Heaviside function

$$H(x) = \begin{cases} 1 & x \geq 0, \\ 0 & x < 0. \end{cases} \tag{3.10}$$

The expressions of the two projection tensors $\mathbb{P}^+$ and $\mathbb{P}^-$ are based on the work by Miehe and Lambrecht [52, 53]. First, a fourth-order tensor is defined as

$$\mathbb{G}_{\alpha\beta} = \boldsymbol{n}_\alpha \otimes \boldsymbol{n}_\beta \otimes \boldsymbol{n}_\alpha \otimes \boldsymbol{n}_\beta + \boldsymbol{n}_\alpha \otimes \boldsymbol{n}_\beta \otimes \boldsymbol{n}_\beta \otimes \boldsymbol{n}_\alpha.$$

For the expression of $\mathbb{P}^+$, we introduce the scalar

$$\vartheta_{\alpha\beta}^{+} = \begin{cases} \dfrac{\langle \epsilon_\alpha \rangle_+ - \langle \epsilon_\beta \rangle_+}{\epsilon_\alpha - \epsilon_\beta}, & \text{if } \epsilon_\alpha \neq \epsilon_\beta, \\ \dfrac{H(\epsilon_\alpha) + H(\epsilon_\beta)}{2}, & \text{if } \epsilon_\alpha = \epsilon_\beta. \end{cases}$$

Then,

$$\mathbb{P}^+ = \frac{\partial \boldsymbol{\epsilon}^+}{\partial \boldsymbol{\epsilon}} = \sum_\alpha H(\epsilon_\alpha) \mathbf{M}_\alpha \otimes \mathbf{M}_\alpha + \frac{1}{2} \sum_\alpha \sum_{\beta \neq \alpha} \vartheta_{\alpha\beta}^{+} \frac{\mathbb{G}_{\alpha\beta} + \mathbb{G}_{\beta\alpha}}{2}.$$

For the expression of $\mathbb{P}^-$, we introduce the scalar

$$\vartheta_{\alpha\beta}^{-} = \begin{cases} \dfrac{\langle \epsilon_\alpha \rangle_- - \langle \epsilon_\beta \rangle_-}{\epsilon_\alpha - \epsilon_\beta}, & \text{if } \epsilon_\alpha \neq \epsilon_\beta, \\ \dfrac{H(-\epsilon_\alpha) + H(-\epsilon_\beta)}{2}, & \text{if } \epsilon_\alpha = \epsilon_\beta. \end{cases}$$

Then,

$$\mathbb{P}^- = \frac{\partial \boldsymbol{\epsilon}^-}{\partial \boldsymbol{\epsilon}} = \sum_\alpha H(-\epsilon_\alpha) \mathbf{M}_\alpha \otimes \mathbf{M}_\alpha + \frac{1}{2} \sum_\alpha \sum_{\beta \neq \alpha} \vartheta_{\alpha\beta}^{-} \frac{\mathbb{G}_{\alpha\beta} + \mathbb{G}_{\beta\alpha}}{2}.$$

The fourth-order projection tensors $\mathbb{P}^+$ and $\mathbb{P}^-$ have the following properties:

$$\mathbb{P}^+ : \boldsymbol{\epsilon} = \boldsymbol{\epsilon}^+, \quad \mathbb{P}^+ : \boldsymbol{\epsilon}^+ = \boldsymbol{\epsilon}^+, \quad \mathbb{P}^- : \boldsymbol{\epsilon} = \boldsymbol{\epsilon}^-, \quad \mathbb{P}^- : \boldsymbol{\epsilon}^- = \boldsymbol{\epsilon}^-$$

and

$$\mathbb{P}^+ : \boldsymbol{\epsilon}^- = \mathbf{0}, \quad \mathbb{P}^- : \boldsymbol{\epsilon}^+ = \mathbf{0}.$$

In an intact material, the elastic energy density function can be expressed by the strain tensor $\boldsymbol{\varepsilon}$ as

$$\psi(\boldsymbol{\varepsilon}) = \frac{1}{2} \lambda tr^2 \boldsymbol{\varepsilon} + \mu \boldsymbol{\varepsilon} : \boldsymbol{\varepsilon},$$

where λ and μ are the Lamé parameters, and tr$\boldsymbol{\epsilon}$ is the trace of the strain tensor. Using the decomposition of the strain tensor, ψ can be simultaneously decomposed into the tensile and the compression parts as

$$\psi^{\pm}(\boldsymbol{\varepsilon}) = \frac{1}{2} \lambda \langle tr \boldsymbol{\varepsilon} \rangle_{\pm}^2 + \mu \boldsymbol{\varepsilon}^{\pm} : \boldsymbol{\varepsilon}^{\pm}. \tag{3.11}$$

Based on the degraded strain energy function in Eq. (3.5), the stress tensor is expressed as

$$\boldsymbol{\sigma} = \frac{\partial \psi(\boldsymbol{\varepsilon}, d)}{\partial \varepsilon} = g(d) \boldsymbol{\sigma}^+ + \boldsymbol{\sigma}^-, \tag{3.12}$$

where

$$\boldsymbol{\sigma}^{\pm} = \lambda tr \langle \boldsymbol{\varepsilon} \rangle_{\pm} \boldsymbol{I} + 2\mu \boldsymbol{\varepsilon}^{\pm}. \tag{3.13}$$

The stress-strain tensor $\mathbb{D}$ is defined as [54, 55]

$$\mathbb{D} = \frac{\partial \boldsymbol{\sigma}}{\partial \boldsymbol{\varepsilon}} = g(d)\frac{\partial \boldsymbol{\sigma}^+}{\partial \boldsymbol{\varepsilon}} + \frac{\partial \boldsymbol{\sigma}^-}{\partial \boldsymbol{\varepsilon}} = g(d)\mathbb{D}^+ + \mathbb{D}^- \tag{3.14}$$

where

$$\mathbb{D}^{\pm} = \lambda H(\pm tr\boldsymbol{\varepsilon})\boldsymbol{I} \otimes \boldsymbol{I} + 2\mu\mathbb{P}^{\pm} \tag{3.15}$$

and $\boldsymbol{I}$ is the second-order identity tensor.

3.1.5 History strain energy

According to the second law of thermodynamics, as the external load is released, the crack should not heal itself. Thus, the phase-field irreversibility conditions needs to be enforced. In this work, the so-called history variable approach is adopted [24]. The history variable is defined as

$$\mathcal{H}(\boldsymbol{x}, t) = \max_{s\in[0,t]} \psi^+(\boldsymbol{\epsilon}(\boldsymbol{x}, s)). \tag{3.16}$$

Numerically this history field enforces the crack propagation irreversibility condition, which will be shown later.

3.2 Weak form and finite element formulation

Based on the total energy functional and the variational principle, the weak form could be derived. Based on the weak form, the finite element method is adopted to obtain the discretized linear system.

3.2.1 Construction of the weak form

The variational approach can be applied to the minimization problem shown in Eq. (3.4).

$$\begin{aligned}
\delta\Pi &= D_{\delta\boldsymbol{u},\delta d}\Pi(\boldsymbol{u}, d) \\
&= \frac{d}{d\epsilon}\bigg|_{\epsilon=0} \Pi(\boldsymbol{u} + \epsilon\delta\boldsymbol{u}, d + \epsilon\delta d) \\
&= \int_\Omega (\frac{\partial\psi}{\partial\boldsymbol{\varepsilon}} : \boldsymbol{\varepsilon}(\delta\boldsymbol{u}) + \frac{\partial\psi}{\partial d}\delta d)dV + \int_\Omega (\frac{g_c}{l}d\delta d + g_c l\nabla d\cdot\nabla\delta d)dV \\
&- \int_\Omega \boldsymbol{b}\cdot\delta\boldsymbol{u}dV - \int_{\partial\Omega}\boldsymbol{p}\cdot\delta\boldsymbol{u}dA \\
&= (\nabla^s\delta\boldsymbol{u}, \boldsymbol{\sigma}) - (\delta\boldsymbol{u}, \boldsymbol{b}) - (\delta\boldsymbol{u}, \boldsymbol{p})_{\partial\Omega} + (\delta d, \frac{g_c}{l}d) + (\nabla\delta d, g_c l\nabla d) + (\delta d, g'(d)\psi^+)
\end{aligned}$$

In the above calculation, the partial derivative of Eq. (3.5) gives

$$\frac{\partial \psi}{\partial d} = g'(d)\psi^+.$$

Considering the history variable approach to enforce the phase-field irreversibility condition, ψ^+ is replaced by the history field variable $\mathcal{H}$. Therefore, the modified first-order variation of the total energy functional is obtained as

$$\delta \Pi = (\nabla^s \delta \boldsymbol{u}, \boldsymbol{\sigma}) - (\delta \boldsymbol{u}, \boldsymbol{b}) - (\delta \boldsymbol{u}, \boldsymbol{p})_{\partial\Omega} + (\delta d, \frac{g_c}{l} d) + (\nabla \delta d, g_c l \nabla d) + (\delta d, g'(d)\mathcal{H}). \quad (3.17)$$

3.2.2 Euler-Lagrange equations

The integral terms in the weak form can be further expanded with the divergence theorem

$$\begin{aligned}
\int_\Omega \frac{\partial \psi}{\partial \varepsilon} \delta\varepsilon dV &= \int_\Omega \sigma_{ij} \delta\varepsilon_{ij} dV \\
&= \int_\Omega \sigma_{ij} \frac{\delta u_{i,j} + \delta u_{j,i}}{2} dV \\
&= \int_\Omega \sigma_{ij} \delta u_{i,j} dV \\
&= -\int_\Omega \sigma_{ij,j} \delta u_i dV + \int_\Omega (\sigma_{ij} \delta u_i)_{,j} dV \\
&= -\int_\Omega \nabla \cdot \boldsymbol{\sigma} \delta \boldsymbol{u} dV + \int_{\partial\Omega} \boldsymbol{\sigma} \cdot \boldsymbol{n} \delta \boldsymbol{u} dA
\end{aligned}$$

and

$$\begin{aligned}
\int_\Omega g_c l \nabla d \nabla \delta d dV &= g_c l \int_\Omega d_{,i} \delta d_{,i} dV \\
&= g_c l \int_\Omega (\delta d d_{,i})_{,i} dV - g_c l \int_\Omega \delta d d_{,ii} dV \\
&= g_c l \int_{\partial\Omega} \nabla d \cdot \boldsymbol{n} \delta d dA - g_c l \int_\Omega \nabla^2 d \delta d dV
\end{aligned} \quad .$$

The weak form shown in Eq. (3.17) can be expressed as

$$\begin{aligned}
\delta \Pi(\boldsymbol{u}, d) = &-\int_\Omega [\nabla \cdot [g(d)\boldsymbol{\sigma}^+ + \boldsymbol{\sigma}^-] + \boldsymbol{b}] \delta \boldsymbol{u} \mathrm{d}V + \int_{\partial\Omega} [(g(d)\boldsymbol{\sigma}^+ + \boldsymbol{\sigma}^-) \cdot \boldsymbol{n} - \boldsymbol{p}] \delta \boldsymbol{u} \mathrm{d}A \\
&+ \int_\Omega [g'(d)\mathcal{H} + \frac{g_c}{l}(d - l^2 \nabla^2 d)] \delta d \mathrm{d}V + \int_{\partial\Omega} g_c l \nabla d \cdot \boldsymbol{n} \delta d \mathrm{d}A
\end{aligned} \quad (3.18)$$

Therefore, the Euler-Lagrange equations obtained from the variational principle of the total energy functional can be expressed as the governing partial differential equations

and the corresponding boundary conditions of the phase-field and the displacement field:

$$\begin{cases} g'(d)\mathcal{H} + \frac{g_c}{l}(d - l^2\nabla^2 d) = 0 & \text{in } \Omega \\ \nabla \cdot [g(d)\boldsymbol{\sigma}^+ + \boldsymbol{\sigma}^-] + \boldsymbol{b} = 0 & \text{in } \Omega \end{cases} \tag{3.19a}$$

$$\begin{cases} \nabla d \cdot \boldsymbol{n} = 0 & \text{on } \partial\Omega \\ [g(d)\boldsymbol{\sigma}^+ + \boldsymbol{\sigma}^-] \cdot \boldsymbol{n} = \boldsymbol{p} & \text{on } \partial\Omega_h \\ u = \bar{u} & \text{on } \partial\Omega_u \end{cases} \tag{3.19b}$$

It is noticeable that the degradation function only affects the positive part of the strain energy, making the displacement field in Eq. (3.19a) non-linear, which is known as the anisotropic energy model [25]. In the phase-field equation, the driving force of the phase-field can be defined as

$$F_d = -g'(d)\mathcal{H}, \tag{3.20}$$

that is, the phase-field is driven by the maximum value of the positive strain energy in history.

3.2.3 Finite element discretization

Based on Eq. (3.17), the residuals related to the displacement field and the phase-field are calculated as

$$\boldsymbol{r}_u = (\nabla^s \delta\boldsymbol{u}, \boldsymbol{\sigma}) - (\delta\boldsymbol{u}, \boldsymbol{b}) - (\delta\boldsymbol{u}, \boldsymbol{p})_{\partial\Omega} \tag{3.21a}$$

$$\boldsymbol{r}_d = (\delta d, \frac{g_c}{l} d) + (\nabla\delta d, g_c l \nabla d) + (\delta d, g'(d)\mathcal{H}) \tag{3.21b}$$

Inside a typical Newton-Raphson iteration, the coupled system is linearized as

$$\begin{cases} D_{\Delta u}\boldsymbol{r}_u + D_{\Delta d}\boldsymbol{r}_u = -\boldsymbol{r}_u, \\ D_{\Delta u}\boldsymbol{r}_d + D_{\Delta d}\boldsymbol{r}_d = -\boldsymbol{r}_d, \end{cases} \tag{3.22}$$

where

$$D_{\Delta u}\boldsymbol{r}_u = (\nabla^s \delta\boldsymbol{u}, \frac{\partial\boldsymbol{\sigma}}{\partial\boldsymbol{\varepsilon}} : \boldsymbol{\varepsilon}(\Delta\boldsymbol{u})),$$

$$D_{\Delta d}\boldsymbol{r}_u = (\nabla^s \delta\boldsymbol{u}, \frac{\partial\boldsymbol{\sigma}}{\partial d} : \Delta d),$$

$$D_{\Delta u}\boldsymbol{r}_d = (\delta d, g'(d)\frac{\partial\mathcal{H}}{\partial\boldsymbol{\varepsilon}} : \boldsymbol{\varepsilon}(\Delta\boldsymbol{u})),$$

$$D_{\Delta d}\boldsymbol{r}_d = (\delta d, ((\frac{g_c}{l} + g''(d)\mathcal{H}))\Delta d) + (\nabla\delta d, g_c l \nabla(\Delta d)).$$

The computational domain is discretized by a finite mesh. Using the shape functions, the displacement field and the phase-field can be expressed as

$$\boldsymbol{u}^h = \sum_A N_{uA}(x)\boldsymbol{u}_A, \tag{3.24a}$$

$$d^h = \sum_A N_{dA}(x)d_A, \tag{3.24b}$$

and their gradients are discretized as

$$\boldsymbol{\varepsilon}^h = \sum_A \boldsymbol{B}_A(x)\boldsymbol{u}_A, \tag{3.25a}$$

$$\nabla d^h = \sum_A \nabla N_{dA}(x)d_A, \tag{3.25b}$$

where the matrices $\boldsymbol{N}_u, \nabla N_d$ and $\boldsymbol{B}$ are defined as

$$\boldsymbol{N}_{uA}(x) = \begin{bmatrix} N_{uA} & 0 & 0 \\ 0 & N_{uA} & 0 \\ 0 & 0 & N_{uA} \end{bmatrix},$$

$$\nabla N_{dA}(\boldsymbol{x}) = \begin{bmatrix} \frac{\partial N_{dA}}{\partial x} & \frac{\partial N_{dA}}{\partial y} & \frac{\partial N_{dA}}{\partial z} \end{bmatrix}^T,$$

$$\boldsymbol{B}_A(\boldsymbol{x}) = \begin{bmatrix} \frac{\partial N_A^u}{\partial x} & 0 & 0 \\ 0 & \frac{\partial N_A^u}{\partial y} & 0 \\ 0 & 0 & \frac{\partial N_A^u}{\partial z} \\ \frac{\partial N_A^u}{\partial y} & \frac{\partial N_A^u}{\partial x} & 0 \\ 0 & \frac{\partial N_A^u}{\partial z} & \frac{\partial N_A^u}{\partial y} \\ \frac{\partial N_A^u}{\partial z} & 0 & \frac{\partial N_A^u}{\partial x} \end{bmatrix}.$$

Based on the linearization shown in Eq. (3.22), inside a Newton-Raphson iteration, the solution update can be written as

$$\begin{bmatrix} \boldsymbol{u}^{(k+1)} \\ d^{(k+1)} \end{bmatrix} = \begin{bmatrix} \boldsymbol{u}^{(k)} \\ d^{(k)} \end{bmatrix} + \begin{bmatrix} K_{uu}^{(k)} & K_{ud}^{(k)} \\ K_{du}^{(k)} & K_{dd}^{(k)} \end{bmatrix}^{-1} \begin{bmatrix} -\boldsymbol{r}_u^{(k)} \\ -\boldsymbol{r}_d^{(k)} \end{bmatrix}. \tag{3.27}$$

The finite element form can be obtained by replacing test functions in the weak form with the shape functions,

$$K_{uu} = \int_\Omega \boldsymbol{B}_A^T[g(d)\mathbb{D}^+ + \mathbb{D}^-]\boldsymbol{B}_B dV, \tag{3.28a}$$

$$K_{ud} = \int_\Omega B_A^T g'(d)\sigma^+ N_{dB} dV, \tag{3.28b}$$

$$K_{du} = \int_\Omega N_A^T g'(d) \frac{\partial \mathcal{H}}{\partial \varepsilon} B_B dV, \tag{3.28c}$$

$$K_{dd} = \int_\Omega g''(d) \mathcal{H} N_{dA}^T N_{dB} dV + \int_\Omega \frac{g_c}{l} N_{dA}^T N_{dB} dV + \int_\Omega g_c l \nabla N_{dA}^T \nabla N_{dB} dV, \tag{3.28d}$$

$$\boldsymbol{r}_u = \int_\Omega \boldsymbol{B}_A^T [g(d)\mathbb{D}^+ + \mathbb{D}^-] \boldsymbol{B}_B dV \boldsymbol{u} - \int_\Omega N_{uA}^T \cdot \boldsymbol{b} dV - \int_{\partial\Omega} N_{uA}^T \cdot \boldsymbol{p} dA, \tag{3.28e}$$

$$\boldsymbol{r}_d = \int_\Omega \frac{g_c}{l} N_{dA}^T N_{dB}^T dV \boldsymbol{d} + \int_\Omega g_c l \nabla N_{dA}^T \nabla N_{dB}^T dV \boldsymbol{d} + \int_\Omega g'(d) \mathcal{H} N_{dA}^T dV. \tag{3.28f}$$

3.3 Solving strategies

Since the total energy functional shown in Eq. (3.2) is non-convex, the conventional Newton-Raphson iterations typically encounter convergence difficulties [37, 38]. In this section, two approaches to solve the above phase-field crack problem are presented. The first approach is based on the so-called alternate minimization [24], which is a type of staggered scheme. The second approach is based on the limited-memory BFGS method [34], which a type of monolithic scheme.

3.3.1 Alternate minimization

To overcome the convergence issues associated with the non-convex energy functional shown in Eq. (3.2), one of the possible approach is based on the so-called alternate minimization (AM) [24], which decomposes the coupled displacement-phase-field problem into two sub-problems. In the first sub-problem, the phase-field is fixed, while the displacement field is updated, that is,

$$\boldsymbol{u}^{(k+1)} = \boldsymbol{u}^{(k)} - {\boldsymbol{K}_{uu}^{(k)}}^{-1} \boldsymbol{r}_u^{(k)}. \tag{3.29}$$

Once the displacement field $\boldsymbol{u}^{(k+1)}$ is obtained, then, the phase-field driving force shown in Eq. (3.20) is updated. Using the new driving force, the residual related to the phase-field equation is further updated to obtain $\boldsymbol{r}_d^{(k+1)}$. Finally, the phase-field is updated as

$$\boldsymbol{d}^{(k+1)} = \boldsymbol{d}^{(k)} - {\boldsymbol{K}_{dd}^{(k)}}^{-1} \boldsymbol{r}_d^{(k+1)}. \tag{3.30}$$

In the alternate minimization approach, the above two equations are solved alternately until both residuals related to the displacement field and the phase-field are reduced to the prescribed tolerance. Notice that only Eq. (3.29) related to the displacement field is non-linear due to the degradation function applied to the positive part of the strain energy function. On the other hand, Eq. (3.30) is linear.

3.3.2 L-BFGS scheme

Although the above AM method can overcome the convergence difficulties due to the non-convexity of the phase-field fracture energy functional, the number of iterations to satisfy the convergence criteria can demanding. The Broyden–Fletcher–Goldfarb–Shanno (BFGS) method [56,57] is shown to be effective to solve the phase-field fracture problems in a monolithic way [34,51]. Let $f(\boldsymbol{x})$ represent the total energy functional discretized by the finite element shape functions. The goal of the BFGS method is to find a solution $\boldsymbol{x}^*$ such that the residual $\boldsymbol{r} = \nabla f(\boldsymbol{x}^*) = 0$. In k-th BFGS iteration, let $\boldsymbol{B}_k$ represent approximation of the Hessian matrix and $\boldsymbol{H}_k$ is the inverse of $\boldsymbol{B}_k$, i.e. $\boldsymbol{H}_k = \boldsymbol{B}_k^{-1}$. The main steps of the BFGS method include the following [56,57]:

- Compute the search direction $\boldsymbol{p}_k$

$$\boldsymbol{p}_k = -\boldsymbol{H}_k \boldsymbol{r}_k \tag{3.31}$$

- Update the solution vector $\boldsymbol{x}_{k+1}$

$$\boldsymbol{x}_{k+1} = \boldsymbol{x}_k + \alpha_k \boldsymbol{p}_k \tag{3.32}$$

  in which α_k is step length calculated in a line search procedure.

- Compute intermediate vectors $\boldsymbol{s}_k, \boldsymbol{y}_k$

$$\boldsymbol{s}_k = \boldsymbol{x}_{k+1} - \boldsymbol{x}_k \tag{3.33a}$$

$$\boldsymbol{y}_k = \boldsymbol{r}_{k+1} - \boldsymbol{r}_k \tag{3.33b}$$

- Update matrix $\boldsymbol{H}_{k+1}$

$$\boldsymbol{H}_{k+1} = (\boldsymbol{I} - \rho_k \boldsymbol{s}_k \boldsymbol{y}_k^T)\boldsymbol{H}_k(\boldsymbol{I} - \rho_k \boldsymbol{y}_k \boldsymbol{s}_k^T) + \rho_k \boldsymbol{s}_k \boldsymbol{s}_k^T \tag{3.34}$$

  in which

$$\rho_k = \frac{1}{\boldsymbol{y}_k^T \boldsymbol{s}_k}$$

- Repeat until convergence criteria is satisfied

$$\|\boldsymbol{r}_k\|_2 < tol \tag{3.35}$$

In the line search procedure, the objective function $f(\boldsymbol{x}_{k+1})$ is expected to have a sufficient descent compared with the previous function value $f(\boldsymbol{x}_k)$, so a proper step length α_k is required. The strong Wolfe conditions are used to find the value of α_k.

$$\begin{cases} f(\boldsymbol{x}_k + \alpha_k \boldsymbol{p}_k) \leq f(\boldsymbol{x_k}) + c_1 \alpha_k \boldsymbol{r}_k^T \boldsymbol{p}_k \\ |\boldsymbol{r}(\boldsymbol{x}_k + \alpha_k \boldsymbol{p}_k) \boldsymbol{p}_k| \leq c_2 |\boldsymbol{r}_k^T \boldsymbol{p}_k| \end{cases} . \tag{3.36}$$

The strong Wolfe conditions guarantees that the non-convex function not only has sufficient decrease, but also satisfies the curvature condition

$$\boldsymbol{s}_k^T \boldsymbol{y}_k > 0. \tag{3.37}$$

For the phase-field fracture problem, the function to be minimized is the total energy functional,

$$f(\boldsymbol{x}) = \mathit{\Pi}(\boldsymbol{x})$$

in which $\boldsymbol{x} = [\boldsymbol{u}, \boldsymbol{d}]^T$ is the block vector containing the displacement field and the phase-field. The total energy functional $\mathit{\Pi}(\boldsymbol{x}_{k+1})$ can also be rewritten as a function of the step length α_k in each iteration,

$$\phi(\alpha_k) = \mathit{\Pi}(\boldsymbol{x}_k + \alpha_k \boldsymbol{p}_k) \tag{3.38a}$$

$$\phi'(\alpha_k) = \boldsymbol{r}(\boldsymbol{x}_k + \alpha_k \boldsymbol{p}_k)^T \boldsymbol{p}_k. \tag{3.38b}$$

Based Eqs. (3.36) and Eq. (3.38), the strong Wolfe conditions are recast as

$$\begin{cases} \phi(\alpha_k) \leq \phi(0) + c_1 \alpha_k \phi'(0) \\ \phi'(\alpha_k) \leq c_2 \, |\phi'(0)| \end{cases} \tag{3.39}$$

The theory of the strong Wolfe conditions [58] can be illustrated in Fig. 3.1. Assume that the black curve in Fig. 3.1 $\phi(\alpha_k)$ is in the current search procedure. When $\alpha_k = 0$, $\phi(0) = f(\boldsymbol{x}_k)$, this is the target function value corresponding to current solution. After this line search procedure, the target function value should be lower than current $\phi(0)$. The exact descent value in a search procedure is difficult to be determined. Alternately, the gradient information at current solution can be used. The derivative at $\alpha_k = 0$ is $\phi'(0) = \boldsymbol{r}_k^T \boldsymbol{p}_k$. Let $0 < c_1 < 1$, the expression of the yellow dash line is then $\phi = \phi(0) + c_1 \phi'(0) \alpha_k$. Any value lower than this yellow dash line on the curve is considered satisfying the sufficient descent conduction. As shown in Fig. 3.1, if α_k is too small, the value of $\phi(\alpha_k)$ is still lower than the yellow dash line, however, the absolute value of descent is not enough. At very small α_k value, the gradient of $\phi(\alpha_k)$ is still large, thus it can still decrease with increment of α_k. When the gradient of $\phi(\alpha_k)$ decreased to $c_2 \phi'(0)$,

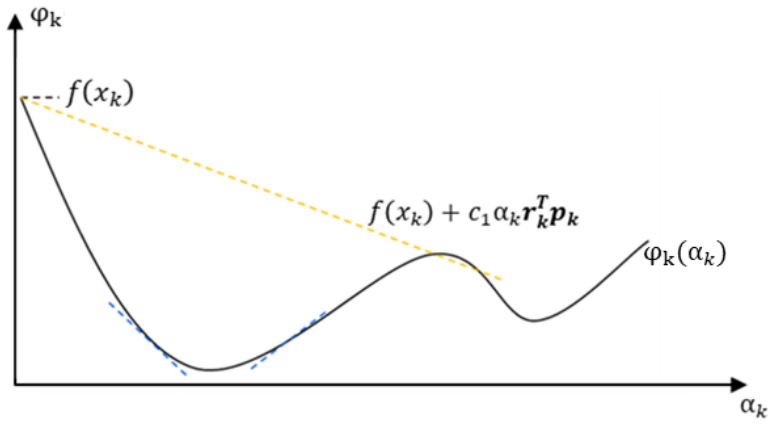

Figure 3.1: Theory of strong Wolfe conditions

where $c_1 < c_2 < 1$ is adopted to prevent the gradient in each search procedure has too large fluctuation, the descent of target function in current search procedure is considered enough. However, if α_k is too large, it might exceed the minimum point, thus, the absolute value is applied, $\phi(\alpha_k) \leq c_2 \left|\phi'(0)\right|$, which is shown by the two blue dash lines.

The disadvantage of the conventional BFGS method is that the fully dense Hessian matrix has to be stored, making the requirement of memory impractical. Thus, it is necessary to improve the algorithm to save the required computer memory. To achieve the limited-memory feature, inside the k-th iteration, the search direction shown in Eq. (3.31) is calculated via a two-loop recursive process, as shown in Algorithm 3.1. Instead of storing the full dense $n \times n$ Hessian matrix, only a few vectors of size n are stored. In this algorithm, an integer $\hat{m} = \min(m, k)$ is defined, where m represent the maximum number of vector pairs.

Algorithm 3.1 Two-loop recursive process to calculate the search direction inside the k-th iteration [34] .

Input:

residual $\boldsymbol{r}_k$

$\hat{m} = min\{m, k\}$
for $i = k-1, ..., k-\hat{m}$ **do**
    calculate $\rho_i = \frac{1}{\boldsymbol{y}_i^T \boldsymbol{s}_i}$
    calculate $\alpha_i = \rho_i \boldsymbol{s}_i^T \boldsymbol{r}_k$
    $\boldsymbol{r}_k \leftarrow \boldsymbol{r}_k - \alpha_i \boldsymbol{y}_i$
end for
$\boldsymbol{p}_k = \boldsymbol{H}_k^0 \boldsymbol{r}_k$
for $i = k-\hat{m}, ..., k-1$ **do**
    $\beta = \rho_i \boldsymbol{y}_i^T \boldsymbol{p}_k$
    $\boldsymbol{p}_k \leftarrow \boldsymbol{p}_k + \boldsymbol{s}_i(\alpha_i - \beta)$
end for
$\boldsymbol{p}_k \leftarrow -1 \times \boldsymbol{p}_k$
return $\boldsymbol{p}_k$

3.3.3 Algorithms

The algorithms for the alternate minimization and the limited-memory BFGS method are provided in the Algorithms 3.2, 3.3, and 3.4. These algorithms are implemented in deal.II [48], which is an open-source C++ finite element library. All the source codes and input files used in this thesis can be found on GitHub[1].

3.4 Thermal-induced cracks

In many engineering systems, such as the thermal barrier coating that is widely used in aerospace engineering, cracks are induced not only by mechanical loading but also thermal effects. The phase-field crack simulation can incorporate the thermal responses by introducing the thermal conduction problem into the coupled system. In this section, the computational framework of the phase-field crack simulation is expanded to take the thermal effects into consideration.

[1] https://github.com/taojinllnl/

Algorithm 3.2 Phase-field fracture algorithm inside a load step

Input:

$t, \Delta t$ ▷ simulation time, step size

necessary information ▷ meshing, materials properties,...

Output:

solution vectors $\boldsymbol{u}_{n+1}$,$\boldsymbol{d}_{n+1}$ or block solution vector $[\boldsymbol{u}_{n+1}$,$\boldsymbol{d}_{n+1}]^T$

for $t_n = 0, \Delta t, ..., t - \Delta t$ **do** ▷ time steps
  if AM used **then**
    $\boldsymbol{u}_k \leftarrow \boldsymbol{u}_n, \boldsymbol{d}_k \leftarrow \boldsymbol{d}_n$ ▷ initialize solution vectors for AM iterations
  else if L-BFGS used **then**
    $[\boldsymbol{u}_k, \boldsymbol{d}_k]^T \leftarrow [\boldsymbol{u}_n, \boldsymbol{d}_n]^T$ ▷ initialize block solution vector for L-BFGS iterations
  end if
  for $k = 1, ..., k_{max}$ **do**
    if AM used **then**
      call Algo. 3.3
    else if L-BFGS used **then**
      call Algo. 3.4
    end if
    calculate $\Delta \Pi$ ▷ increment of energy
    if $\Delta \Pi < tol$ **then**
      break
    end if
  end for
  if AM used **then**
    $\boldsymbol{u}_{n+1} \leftarrow \boldsymbol{u}_k, \boldsymbol{d}_{n+1} \leftarrow \boldsymbol{d}_k$ ▷ update values at current time step
    return $\boldsymbol{d}_{n+1}, \boldsymbol{u}_{n+1}$
  else if L-BFGS used **then**
    $[\boldsymbol{u}_{n+1}, \boldsymbol{d}_{n+1}]^T \leftarrow [\boldsymbol{u}_k, \boldsymbol{d}_k]^T$
    return $[\boldsymbol{d}_{n+1}, \boldsymbol{u}_{n+1}]^T$
  end if
  if $\psi^+ > \mathcal{H}$ **then** ▷ update history field
    $\mathcal{H} \leftarrow \psi^+$
  else
    $\mathcal{H} \leftarrow \mathcal{H}$
  end if
end for

Algorithm 3.3 Alternate minimization in the k-th iteration

Input:

solution vectors at beginning of iteration $\boldsymbol{u}_k, \boldsymbol{d}_k$

i_{max}, tol ▷ max Newton-Raphson iteration and tolerance of residual

Output:

$\boldsymbol{u}_{k+1}, \boldsymbol{d}_{k+1}$

for $i = 1, ..., i_{max}$ **do** ▷ Newton-Raphson method for non-linear displacement field
  calculate $\boldsymbol{u}_k^i$ using Eq. (3.29)
  if $\boldsymbol{r}_u < tol$ **then**
    $\boldsymbol{u}_{k+1} = \boldsymbol{u}_k^i$
    break
  end if
end for
calculate $\boldsymbol{d}_{k+1}$ using Eq. (3.30) ▷ linear equation is only solved once
return $\boldsymbol{u}_{k+1}, \boldsymbol{d}_{k+1}$

Algorithm 3.4 L-BFGS algorithm in the k-th iteration

Input:

solution vector at beginning of iteration $\boldsymbol{x}_k$ ▷ $\boldsymbol{x}_k = [\boldsymbol{u}_k, \boldsymbol{d}_k]^T$ in this problem

Output: $\boldsymbol{x}_{k+1}$

calculate residual $\boldsymbol{r}_k$
call Algo. 3.1 to calculate search direction $\boldsymbol{p}_k$
calculate $\phi(0) = \Pi(\boldsymbol{x}_k)$ and $\phi'(0) = \boldsymbol{r}_k \boldsymbol{p}_k$
calculate line search parameter α_k satisfying strong Wolfe conditions
calculate increment $\Delta \boldsymbol{x} = \alpha_k \boldsymbol{p}_k$, and $\boldsymbol{x}_{k+1} = \boldsymbol{x}_k + \Delta \boldsymbol{x}$
if $k > m$ **then**
  Remove vector pair $\{s_{k-m}, y_{k-m}\}$
end if
calculate inverse of Hessian matrix $\boldsymbol{H}_{k+1}$
add vector pair $\{s_k, y_k\}$
return $\boldsymbol{x}_{k+1}$

3.4.1 Heat conduction problem

The evolution and distribution of the temperature field $T(\boldsymbol{x}, t)$ are expressed by the following partial differential equation:

$$c\rho\frac{\partial T}{\partial t} = \boldsymbol{\kappa}\nabla^2 T + q, \tag{3.40}$$

where c is the specific heat capacity, ρ is the material density, $\boldsymbol{\kappa}$ is the heat conductivity tensor, and q is the heat source. Introducing the test function δT, the weak form of the above equation can be obtained as

$$\int_\Omega \delta T c\rho\frac{\partial T}{\partial t}dV + \int_\Omega \delta\nabla T\boldsymbol{\kappa}\nabla T dV = \int_\Omega \delta T q dV - \int_{\partial\Omega}\delta T\boldsymbol{J}\cdot\boldsymbol{n}dA \tag{3.41}$$

where $\boldsymbol{J}$ is the heat flux at the domain boundary defined as

$$\boldsymbol{J} = -\boldsymbol{\kappa}\nabla T. \tag{3.42}$$

Using the standard finite element method and the backward Euler method, the above weak form can be solved to obtain the temperature field when the Dirichlet and Neumann boundary conditions as well as the initial conditions are provided.

3.4.2 Thermal stress

The temperature distribution in the computational domain generates the so-called thermal strain, which subsequently causes changes in the stress distribution. The thermal strain can be calculated as

$$\boldsymbol{\varepsilon}_T = \alpha(T - T_{ref})\boldsymbol{I}, \tag{3.43}$$

where T_{ref} is the reference temperature, α is the thermal expansion coefficient, and $\boldsymbol{I}$ is the second-order identity tensor. Considering the thermal effect, the total stress is then modified as

$$\boldsymbol{\sigma} = \mathbb{D}(\boldsymbol{\varepsilon} - \boldsymbol{\varepsilon}_T), \tag{3.44}$$

where $\mathbb{D}$ is the 4-th order material elasticity tensor. Introducing the thermal stress, the weak form of the balance of the linear momentum is modified as

$$\int_\Omega \mathbb{D}(\boldsymbol{\varepsilon} - \boldsymbol{\varepsilon_T})\delta\boldsymbol{\varepsilon}dV - \int_\Omega \boldsymbol{b}\cdot\delta\boldsymbol{u}dV - \int_{\partial\Omega}\boldsymbol{p}\cdot\delta\boldsymbol{u}dA = 0, \tag{3.45}$$

where $\boldsymbol{b}$ represents the body force and $\boldsymbol{p}$ represents the surface traction force. After considering the thermal effect in the thermal strain, the strain decomposition is performed as before to obtain the tensile part and compression part. Then, the procedures described in Section 3.2 are followed for the phase-field crack simulation.

3.4.3 Solving strategy of thermal-induced phase-field problem

Generally speaking, after considering the thermal effects, the phase-field crack simulation becomes a three-field coupled problem that includes the displacement field $\boldsymbol{u}$, the phase-field d, and the temperature field T. Inside the k-th nonlinear iteration, the solution can be updated according to the following incremental form,

$$\begin{bmatrix} \boldsymbol{u}^{(k+1)} \\ d^{(k+1)} \\ T^{(k+1)} \end{bmatrix} = \begin{bmatrix} \boldsymbol{u}^{(k)} \\ d^{(k)} \\ T^{(k)} \end{bmatrix} + \begin{bmatrix} K_{uu}^{(k)} & K_{ud}^{(k)} & K_{uT}^{(k)} \\ K_{du}^{(k)} & K_{dd}^{(k)} & K_{dT}^{(k)} \\ K_{Tu}^{(k)} & K_{Td}^{(k)} & K_{TT}^{(k)} \end{bmatrix}^{-1} \begin{bmatrix} -\boldsymbol{r}_u^{(k)} \\ -\boldsymbol{r}_d^{(k)} \\ -\boldsymbol{r}_T^{(k)} \end{bmatrix}. \tag{3.46}$$

In this work, it is assumed that the displacement field and the phase-field have no impact on the temperature field [59]. Therefore, some of the off-diagonal terms in the above block matrix are zero, that is,

$$K_{Tu}^{(k)} = K_{Td}^{(k)} = 0.$$

Furthermore, it is assumed that the temperature field has no direct impact on the phase-field, and therefore,

$$K_{dT}^{(k)} = 0.$$

Considering the above assumptions, the coupled nonlinear iteration becomes

$$\begin{bmatrix} \boldsymbol{u}^{(k+1)} \\ d^{(k+1)} \\ T^{(k+1)} \end{bmatrix} = \begin{bmatrix} \boldsymbol{u}^{(k)} \\ d^{(k)} \\ T^{(k)} \end{bmatrix} + \begin{bmatrix} K_{uu}^{(k)} & K_{ud}^{(k)} & K_{uT}^{(k)} \\ K_{du}^{(k)} & K_{dd}^{(k)} & 0 \\ 0 & 0 & K_{TT}^{(k)} \end{bmatrix}^{-1} \begin{bmatrix} -\boldsymbol{r}_u^{(k)} \\ -\boldsymbol{r}_d^{(k)} \\ -\boldsymbol{r}_T^{(k)} \end{bmatrix}. \tag{3.47}$$

During the finite element formulation, the temperature field is discretized using the same finite element mesh for the phase-field and the displacement. Based on the shape function, the temperature field is expressed as

$$T^h = \sum_A N_{T_A}(x) T_A, \tag{3.48}$$

and its gradient is written as

$$\nabla T^h = \sum_A \nabla N_{T_A}(x) T_A, \tag{3.49}$$

where

$$\nabla N_{TA}(\boldsymbol{x}) = \begin{bmatrix} \frac{\partial N_{TA}}{\partial x} & \frac{\partial N_{TA}}{\partial y} & \frac{\partial N_{TA}}{\partial z} \end{bmatrix}^T.$$

Subsequently, the residual and the stiffness matrix related to the temperature field (heat conduction) are defined as

$$\boldsymbol{r}_T = -\int_\Omega \dot{q} N_{TA}^T dV + \int_{\partial\Omega_J} N_{TA}^T J dA - \int_\Omega \nabla N_{TA}^T \kappa \nabla N_B^T dV \boldsymbol{T} + \boldsymbol{M} \frac{\Delta \boldsymbol{T}}{\Delta t} \tag{3.50}$$

and

$$K_{TT} = \Delta t \int_{\Omega} \nabla N_{TA}^{T} \kappa \nabla N_{TB} dV + \boldsymbol{M}, \tag{3.51}$$

where $\boldsymbol{M}$ is the mass matrix defined as

$$\boldsymbol{M} = \int_{\Omega} c\rho N_{TA}^{T} N_{TB} dV.$$

Moreover, the thermal-mechanical coupling term is defined as [59]

$$K_{uT} = \int_{\Omega} B_{A}^{T} \frac{\partial \boldsymbol{\sigma}}{\partial T} N_{TB} dV. \tag{3.52}$$

Notice that in Eq. (3.47), the stiffness matrix has the non-zero coupling term K_{uT} between the displacement field and the temperature field, making the matrix unsymmetric. The staggered approach is adopted to solve this three-field coupled problem. That is, the full problem is decoupled into two sub-problems. The first sub-problem concerns about the heat conduction, from which the temperature field is obtained. Then, in the second sub-problem, the temperature field is fixed, and the phase-field and the displacement field are obtained simultaneously using the limited-memory BFGS approach represented in Section 3.3. That is, the temperature field is firstly obtained in each time step by solving

$$T^{(k+1)} = T^{(k)} - K_{TT}^{(k)-1} \boldsymbol{r}_{T}^{(k)}, \tag{3.53}$$

which is a linear equation and can be solved using either the direction solvers such as the LU decomposition or the iteration solvers such as the conjugate-gradient method. Then, the second sub-problem in Eq. (3.47) can be expressed as

$$\begin{bmatrix} \boldsymbol{u}^{(k+1)} \\ d^{(k+1)} \end{bmatrix} = \begin{bmatrix} \boldsymbol{u}^{(k)} \\ d^{(k)} \end{bmatrix} + \begin{bmatrix} K_{uu}^{(k)} & K_{ud}^{(k)} \\ K_{du}^{(k)} & K_{dd}^{(k)} \end{bmatrix}^{-1} \begin{bmatrix} -\boldsymbol{r}_{u}^{(k)} \\ -\boldsymbol{r}_{d}^{(k)} \end{bmatrix}. \tag{3.54}$$

Notice that in the above equation, the newly obtained temperature field is fixed and influences the stress field according to Eq. (3.44). Alternatively, the fully coupled three-field problem can be solved according to the fully staggered approach, that is, the whole problem is decomposed into three sub-problems, each of which is related to the temperature field, the displacement field, and the phase-field, separately. Following this fully staggered strategy, the stiffness matrix can be simplified as a 3×3 diagonal matrix [60]. The solving scheme can be further degraded into three sub-equations isolated from each other

$$\begin{aligned} T^{(k+1)} &= T^{(k)} - K_{TT}^{(k)-1} \boldsymbol{r}_{T}^{(k)}, \\ \boldsymbol{u}^{(k+1)} &= \boldsymbol{u}^{(k)} - K_{uu}^{(k)-1} \boldsymbol{r}_{u}^{(k)}, \\ d^{(k+1)} &= d^{(k)} - K_{dd}^{(k)-1} \boldsymbol{r}_{d}^{(k)}. \end{aligned} \tag{3.55}$$

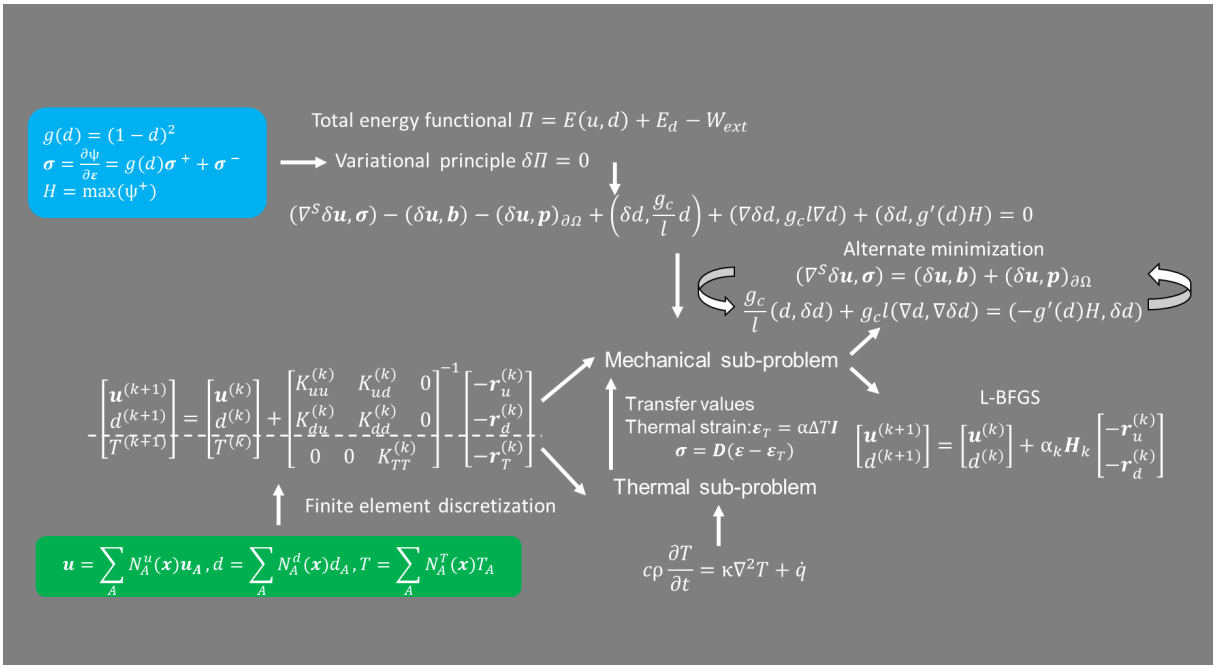

Figure 3.2: Algorithm design for the thermal-induced phase-field crack modeling that involves the temperature, the displacement, and the phase-field.

3.5 Summary

Several algorithms are represented to solve the phase-field crack propagation problems under external loads, such as mechanical loads and thermal loads.Starting from the concept of the total energy functional, the weak form of the phase-field method is constructed by the variational principle. It is a widely adopted assumption that only the tensile principal stresses have effects on the crack propagation, so the spectrum decomposition algorithm is utilized to split the stress. Since the existence of cracks reduces the elastic energy stored in materials, a degradation function is introduced. According to second law of thermodynamics, crack should not self-heal. Therefore, a history field is introduced to enforce the crack propagation irreversibility. Due to the non-convex nature of the total energy functional of the phase-field fracture, the convergence issue is a challenge for numerical simulations. Thus, two solving schemes, the alternate minimization (AM) and the limited-memory BFGS (L-BFGS) are presented. The AM method decouples the system into two sub-problems. It fixes one of the fields while solving for the other until convergence criteria are reached. The L-BFGS method, on the other hand, solves for the coupled fields simultaneously. It solves for the search direction by using an approximated Hessian matrix and deciding a step length in each search procedure via the strong Wolfe conditions. These two algorithms are further combined with a heat conduction problem to

simulate the thermal-induced fracture problems. For the thermal-induced crack problems, the temperature field is firstly isolated from the coupled system. Then, either the staggered or the monolithic approach can be adopted to solve the mechanical sub-problem. Figure 3.2 illustrates the algorithm design and the finite element implementation of the thermal-induced phase-field crack problem.

Chapter 4

Numerical examples

Based on the computational method for the phase-field crack simulation and the corresponding solving strategies, several numerical examples are provided in this chapter. In the first part, several crack propagation problems due to mechanical loading conditions are provided. In the second part, several crack propagation problems due to the thermal effects are presented. All the numerical algorithms and finite element simulations are implemented and performed in deal.II [48], which is an open-source C++ finite element library. All the source codes and input files used in this thesis can be found on GitHub[1].

4.1 Crack propagation caused by mechanical load

In this section, the simulations of crack propagation due to externally applied mechanical loads are provided. The first problem is about the crack propagation under tension. The second problem is about the crack propagation under shear. The third problem is about the crack propagation under bending. The last problem involves the crack propagation in a plane with three unsymmetrical holes to demonstrate the capability of the developed algorithms in dealing with complex geometries. The material properties used in these test cases under mechanical loads are listed in table 4.1.

[1] https://github.com/taojinllnl/

Table 4.1: Material properties for the four test cases under mechanical loading.

Test case	Lamé λ (GPa)	Lamé μ (GPa)	critical energy release rate g_c (kN/mm)
Simple tension test	121.15	80.77	2.7×10^{-3}
Simple shear test	121.15	80.77	2.7×10^{-3}
Simple bending test	6.16	10.95	9.5×10^{-3}
Three-holes test	1.94	2.45	2.28×10^{-3}

If the Young's modulus E and the Poisson's ratio ν are known, then the Lamé parameters λ and μ can be calculated by [61]

$$\lambda = \frac{E\nu}{(1+\nu)(1-2\nu)}, \quad \mu = \frac{E}{2(1+\nu)}. \tag{4.1}$$

If the Lamé parameters λ and μ are known, then the Young's modulus E and the Poisson's ratio ν can be calculated by

$$E = \frac{\mu(3\lambda+2\mu)}{\lambda+\mu}, \quad \nu = \frac{\lambda}{2(\lambda+\mu)}. \tag{4.2}$$

4.1.1 Simple tension test

In this example, a 1.0×1.0 mm specimen with a 0.5 mm preexisting crack is under uniform tensile load. The boundary conditions are applied such that the bottom left corner of the domain is fixed in both x- and y-directions. The bottom edge is fixed in the y-direction, and the top edge is applied with a displacement-controlled load u_y in the y-direction. The phase-field length-scale parameter is chosen as $l = 0.0075$ mm. Since the crack propagation path is known *a priori*, which extends the preexisting crack until it reaches the right edge of the sample, the mesh is pre-refined around the anticipated propagation path.

Figure 4.1 shows the pre-refined finite element mesh and the fully developed crack pattern obtained via the alternate minimization (AM) approach and the limited-memory BFGS (L-BFGS) approach. When the top-edge displacement is $u_y = 6.0 \times 10^{-3}$ mm, the crack propagates abruptly from the tip of the preexisting crack (the center of the domain) to the right edge of the domain. The crack path follows the pre-refined mesh as expected. Figure 4.2 illustrates the normal stress σ_{22} distribution at different loading stages. Before the crack propagation, the stresses almost uniformly increase. After the crack propagation, the stresses are suddenly released.

Figure 4.3 shows the force-displacement relationship of the simple tension test. The sample loses load bearing capacity at the critical load step in which the crack fully develops.

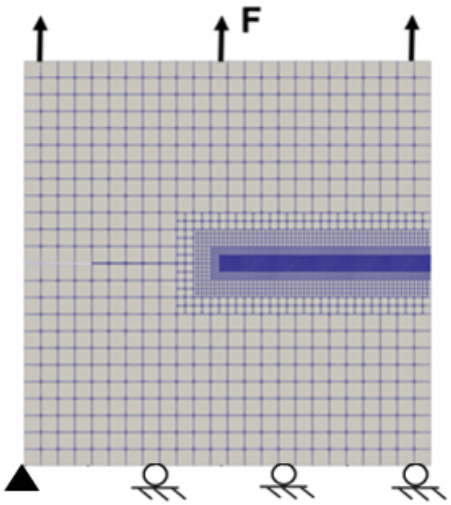

(a) Finite element mesh

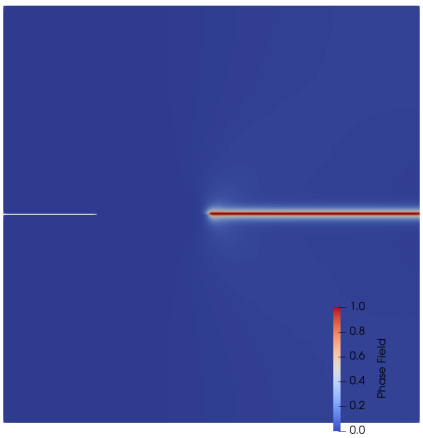

(b) Crack path by AM method

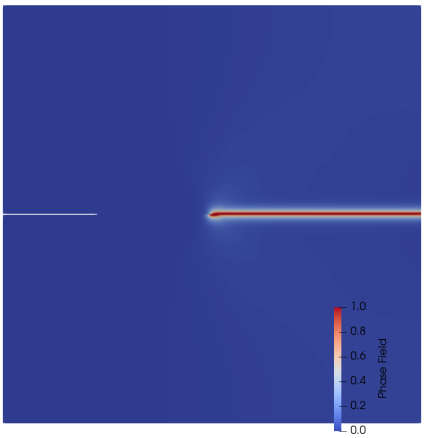

(c) Crack path by L-BFGS method

Figure 4.1: Crack propagation under simple tension inside a unit square (1.0 mm edge length) with a preexisting crack of 0.5 mm long. The preexisting crack is from the center of the left edge to the center of the domain. The boundary conditions are applied such that the bottom left corner of the domain is fixed in both x- and y-directions. The bottom edge is fixed in the y-direction, and the top edge is applied with a displacement-controlled load u_y in the y-direction. The mesh is pre-refined along the anticipated path that is known *a priori*.

Furthermore, the results obtained from the alternate minimization (AM) approach and the limited-memory BFGS (L-BFGS) approach are identical. Due to the non-convexity of the

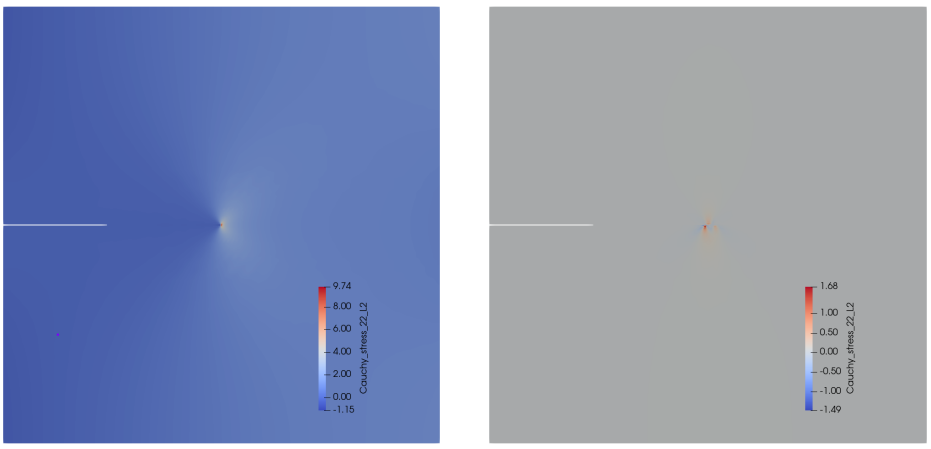

(a) σ_{22} distribution at $u = 0.005$ mm (b) σ_{22} distribution at $u = 0.062$ mm

Figure 4.2: Normal stress σ_{22} (GPa) distribution of simple tension test: Maximum stress gradually increases before crack propagation and suddenly drops after crack propagation.

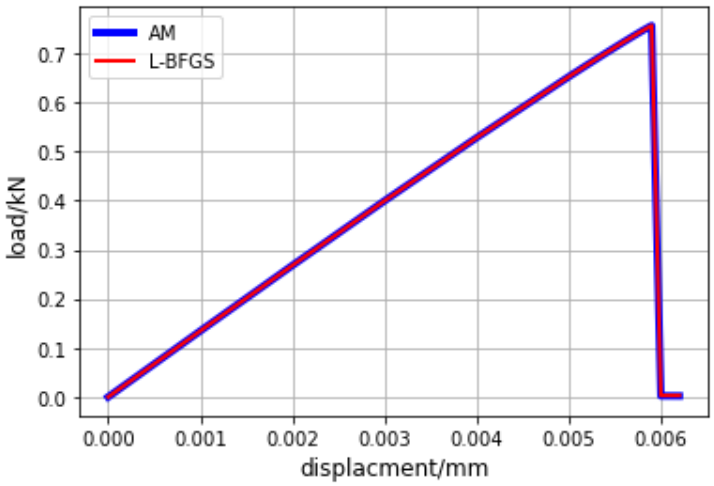

Figure 4.3: Load-displacement relationship of the simple tensile test obtained from the alternate minimization (AM) approach and the limited-memory BFGS (L-BFGS) approach.

total energy functional of the phase-field crack formulation, conventional Newton-Raphson iterations encounter convergence difficulties during the critical load step.

4.1.2 Simple shear test

In this example, the same specimen used in the previous simple tension test is under a shear load. The boundary conditions are applied such that the bottom edge is fixed in both x- and y-directions. The top edge is fixed in the y-direction and is applied with a displacement-controlled load u_x in the x-direction. The phase-field length-scale parameter is chosen as $l = 0.0075$ mm. As shown in Fig. 4.4a, the finite element mesh is pre-refined in the lower-right quarter of the domain where crack is anticipated to propagate. Figures 4.4b and 4.4c show the subsequent crack propagation obtained from the alternate minimization (AM) and the limited-memory BFGS (L-BFGS) approach, respectively.

Figure 4.5 compares the load-displacement relationships obtained from the AM and the L-BFGS approach, which indicate that both methods give similar results. In this loading case, the sample starts to lose the shear load bearing capacity when the horizontal displacement at the top edge reaches to 0.01 mm. Figure 4.6 compares the number of nonlinear iterations required by the L-BFGS approach and the AM approach during each load step in the simple shear test. The former, which is a type of monolithic solving strategy, requires fewer iterations for convergence than the staggered strategy using the alternate minimization (AM).

4.1.3 Simple bending test

In this example, an L-shape sample with the geometrical dimensions shown in Fig. 4.7a is fixed at the bottom edge. A displacement-controlled load is applied upward at a location 30.0 mm to the sample's right edge. Figures 4.7b and 4.7c show the fully developed crack path obtained from the alternate minimization (AM) and the limited-memory BFGS (L-BFGS) approach, respectively. Under the displacement-controlled load that is applied in the vertical direction, the crack initiates at the corner of the L-shape sample and subsequently propagates under the bending load.

The load-displacement curves obtained from the alternate minimization (AM) and the limited-memory BFGS (L-BFGS) approach are compared in Fig. 4.8. After the vertical displacement reaches to 0.24 mm, the L-shape sample starts to lose the load bearing capacity. Figure 4.9 compares the number of nonlinear iterations required by the L-BFGS approach and the AM approach during each load step in the simple bending test. The former, which is a type of monolithic solving strategy, requires fewer iterations for convergence than the staggered strategy using the alternate minimization (AM).

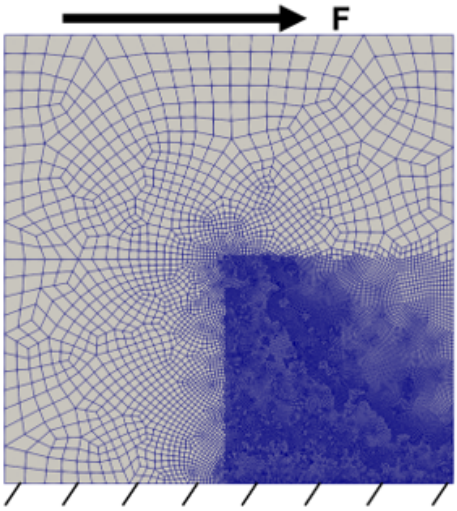

(a) Finite element mesh

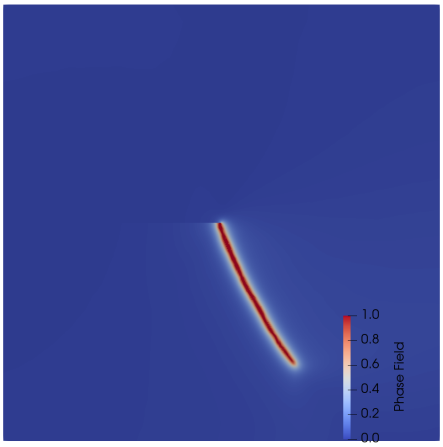

(b) Crack path by AM method

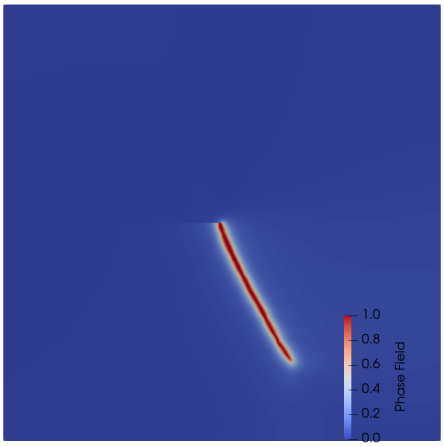

(c) Crack path by L-BFGS method

Figure 4.4: Crack propagation under simple shear inside a unit square (1.0 mm edge length) with a preexisting crack of 0.5 mm long. The preexisting crack is from the center of the left edge to the center of the domain. The boundary conditions are applied such that the bottom edge is fixed in both x- and y-directions. The top edge is fixed in the y-direction and is applied with a displacement-controlled load u_x in the x-direction. The mesh is pre-refined in the region where crack propagation is anticipated.

4.1.4 Plane with unsymmetrical holes

In this case, a plane containing three unsymmetrical holes [62] is used to demonstrate the capability of the phase-field crack algorithms to handle complex geometries. As shown in

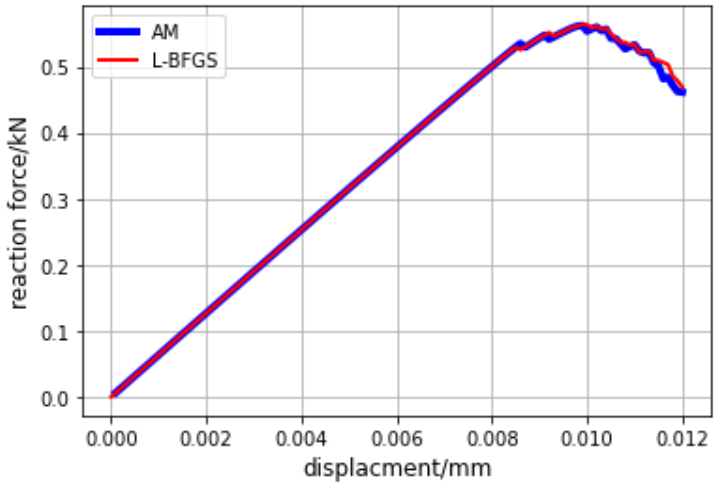

Figure 4.5: Load-displacement relationship of the simple shear test obtained from the alternate minimization (AM) approach and the limited-memory BFGS (L-BFGS) approach.

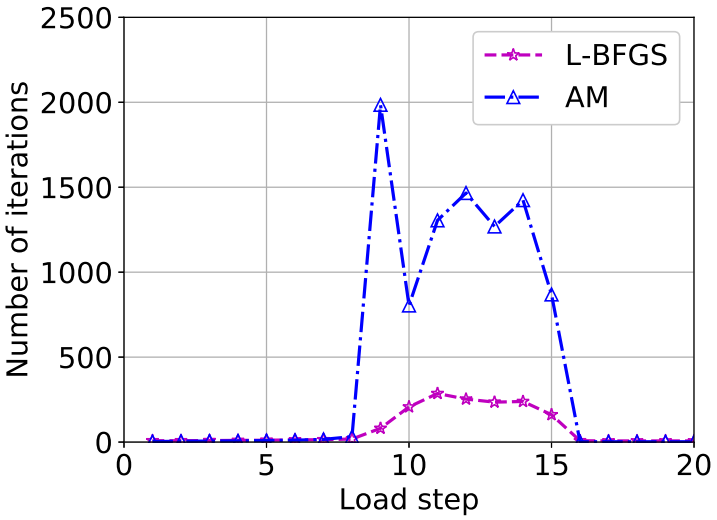

Figure 4.6: Number of iterations required for convergence in each load step in the simple shear test problem. The L-BFGS approach, which is a type of monolithic solving strategy, requires fewer iterations than the staggered approach based on the alternate minimization (AM).

Fig. 4.10a, a vertical load is applied at the top hole, while the bottom hole is constrained in both directions. Figures 4.10b and 4.10c compare the fully developed crack path obtained from the alternate minimization (AM) and the limited-memory BFGS (L-BFGS) approach, respectively. Both solving strategies can successfully capture the relatively complex crack propagation path. Figure 4.11 compares the load-displacement relationships obtained from

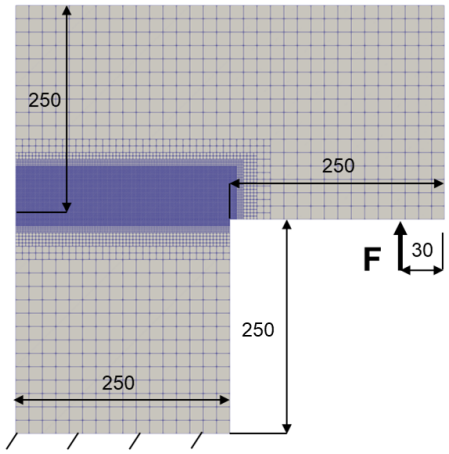

(a) Finite element mesh

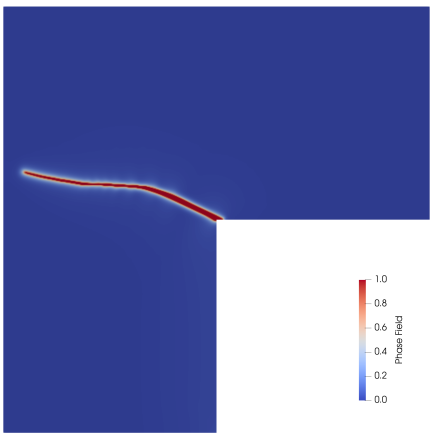

(b) Crack path by AM method

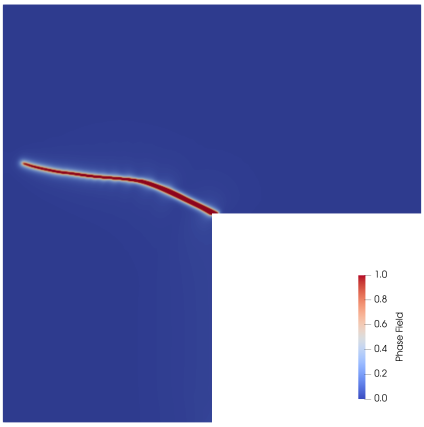

(c) Crack path by L-BFGS method

Figure 4.7: Crack propagation under a displacement-controlled cyclic load in a L-shape sample. The bottom of the sample is fixed, and the displacement-controlled load u_y is applied in the y-direction.

the AM and the L-BFGS approach. These results are similar to the counterpart reported in [62].

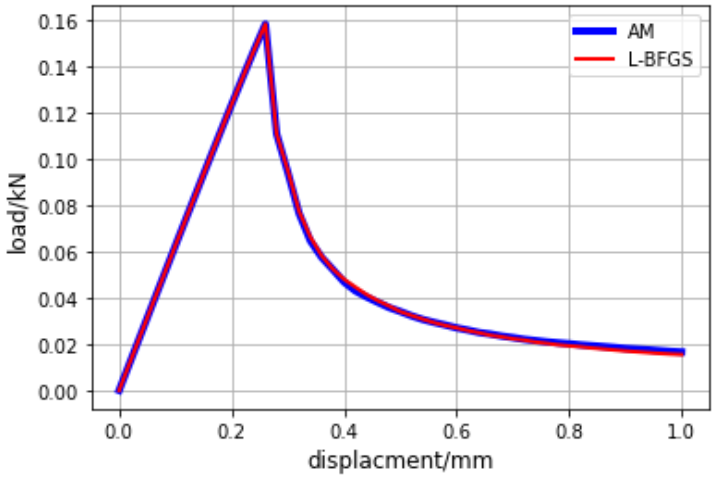

Figure 4.8: Load-displacement relationship of the simple bending test obtained from the alternate minimization (AM) approach and the limited-memory BFGS (L-BFGS) approach.

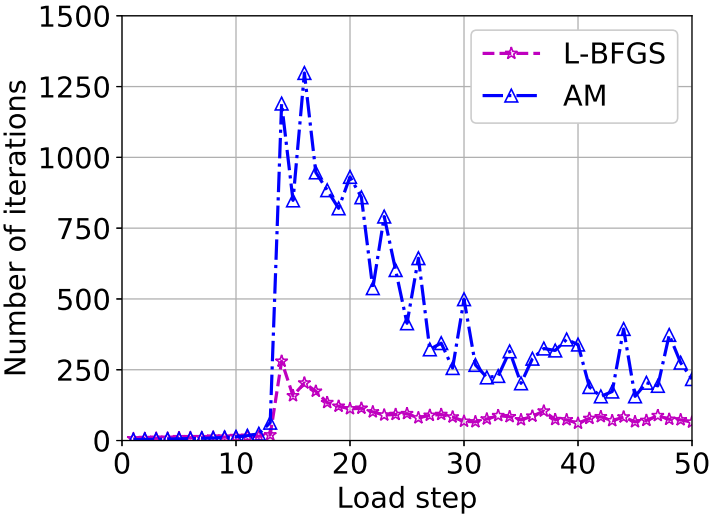

Figure 4.9: Number of iterations required for convergence in each load step in the simple bending test problem. The L-BFGS approach, which is a type of monolithic solving strategy, requires fewer iterations than the staggered approach based on the alternate minimization (AM).

4.2 Thermal-induced crack propagation

In many engineering applications, such as the thermal barrier coatings used in aerospace engineering, cracks are induced by thermal effects. In this section, three numerical examples are provided to demonstrate the capability of the phase-field crack method to model crack propagation due to various thermal effects. Tables 4.2 and 4.3 show the material

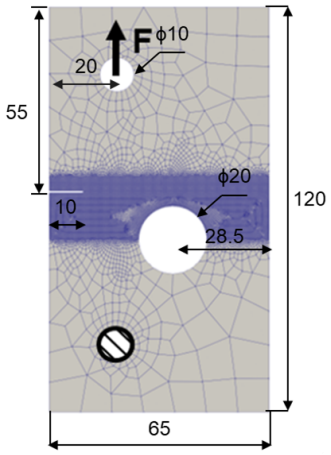

(a) Finite element mesh

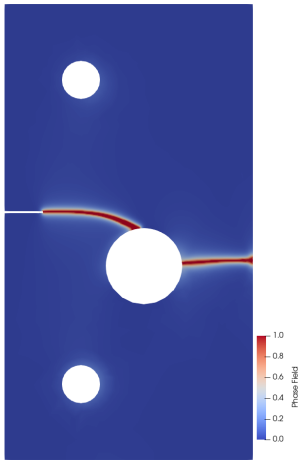

(b) Crack path by AM

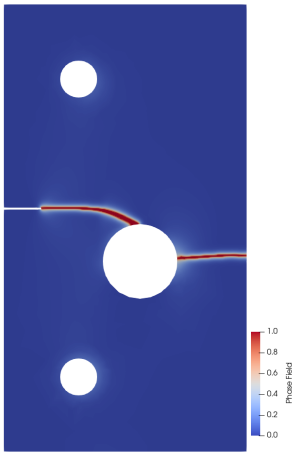

(c) Crack path by L-BFGS

Figure 4.10: Simulation of the crack path in a plane containing three unsymmetrical holes. A vertical load is applied at the top hole, and the bottom hole is fixed in both directions. The phase-field crack simulation based on the alternate minimization (AM) and the limited-memory BFGS (L-BFGS) approach can both capture the complex crack path.

mechanical properties and thermal properties used in the first two numerical examples.

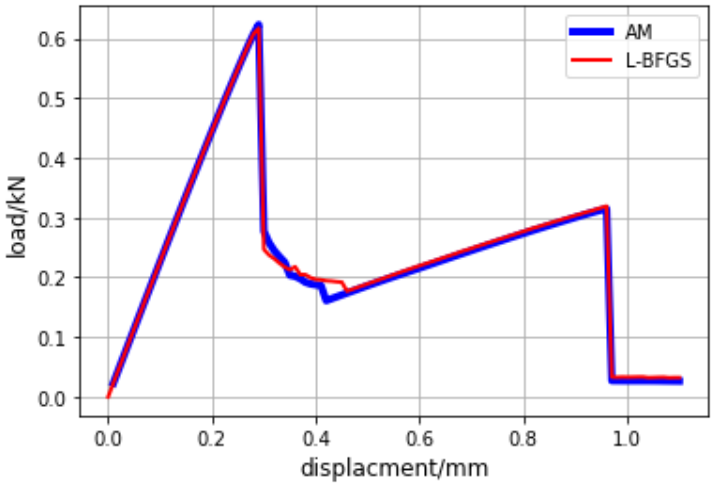

Figure 4.11: Load-displacement curves of the plane containing three holes under the tensile load obtained from the alternate minimization (AM) and the limited-memory BFGS (L-BFGS) method.

Table 4.2: Material mechanical properties for test cases 4.2.1 and 4.2.2

Test case	Lamé λ (GPa)	Lamé μ (GPa)	critical energy release rate g_c (kN/mm)
4.2.1	6.07×10^{-5}	9.1×10^{-5}	2.0×10^{-10}
4.2.2	213.46	143.2	42.5×10^{-6}

Table 4.3: Material thermal properties for test cases 4.2.1 and 4.2.2

Test case No.	CTE α (K^{-1})	conductivity κ ((W/(m· K))	heat capacity c (J/(kg· K))	density ρ (kg/m^3)
4.2.1	6×10^{-4}	1.0	0.0	1.0
4.2.2	7.5×10^{-6}	31.0	880	3980

4.2.1 Crack under imposed thermal gradient

In this case, a cross-shaped specimen is under the effect of an imposed thermal gradient. As shown in Fig. 4.12a, the top edge of the sample is gradually heated from 0.0 ℃ to 10.0 ℃, and the bottom edge of the sample is gradually cooled from 0.0 ℃ to -10.0 ℃. Two different solving strategies are applied to this coupled problem that involves the displacement field, the phase-field, and the temperature field.

In the first solving strategy, the coupled problem is decomposed into three sub-problems. The first sub-problem updates the temperature field while fixing the displacement field and the phase-field. The second sub-problem uses the newly updated temperature field to update the displacement field while keeping the phase-field fixed. The last sub-problem

uses the newly updated temperature field and the displacement field to update the phase-field. Let T, $\boldsymbol{u}$, and d represent the temperature field, the displacement field, and the phase-field, respectively. The solution sequence inside the k-th iteration can be expressed as below:

$$\begin{aligned}
&\text{sub-problem 1:} \quad (T^{(k)}, \boldsymbol{u}^{(k)}, d^{(k)}) \quad &&\longrightarrow \quad (T^{(k+1)}, \boldsymbol{u}^{(k)}, d^{(k)}),\\
&\text{sub-problem 2:} \quad (T^{(k+1)}, \boldsymbol{u}^{(k)}, d^{(k)}) \quad &&\longrightarrow \quad (T^{(k+1)}, \boldsymbol{u}^{(k+1)}, d^{(k)}),\\
&\text{sub-problem 3:} \quad (T^{(k+1)}, \boldsymbol{u}^{(k+1)}, d^{(k)}) \quad &&\longrightarrow \quad (T^{(k+1)}, \boldsymbol{u}^{(k+1)}, d^{(k+1)}).
\end{aligned}$$

In the second solving strategy, the coupled problem is decomposed into two sub-problems. The first sub-problem updates the temperature field while fixing the displacement field and the phase-field. The second sub-problem uses the newly updated temperature field and solve for the displacement field and the phase-field simultaneously using the limited-memory BFGS approach. The solution sequence inside the k-th iteration can be expressed as below:

$$\begin{aligned}
&\text{sub-problem 1:} \quad (T^{(k)}, \boldsymbol{u}^{(k)}, d^{(k)}) \quad &&\longrightarrow \quad (T^{(k+1)}, \boldsymbol{u}^{(k)}, d^{(k)}),\\
&\text{sub-problem 2:} \quad (T^{(k+1)}, \boldsymbol{u}^{(k)}, d^{(k)}) \quad &&\longrightarrow \quad (T^{(k+1)}, \boldsymbol{u}^{(k+1)}, d^{(k+1)}).
\end{aligned}$$

Figures 4.12b and 4.12c compare the crack path obtained from the above two solving strategies, which are both effective to obtain the crack path under the imposed thermal gradient.

4.2.2 Quenching test

In this example, the phase-field crack approach is used to investigate the crack propagation in a quenching test. A 100×10 mm specimen is firstly heated to 280 ℃ and then quenched in a 0 ℃ liquid. Based on the symmetry, only half of the specimen is simulated, as shown in Fig. 4.13b. Since the temperature gradient around the sample boundary is steep, as shown in Fig. 4.13b, considerable thermal-induced stresses are generated in this area, see Fig. 4.14, causing the crack to propagate from the exterior to the interior of the sample. Figure 4.13c shows that multiple cracks propagate from the edges of the sample to the interior, demonstrating the capability of the phase-field method in modeling complex crack patterns induced by the thermal effects.

4.2.3 Crack propagation in thermal barrier coatings

Thermal barrier coatings (TBCs) [63,64] are ceramic layers used to protect substrates that work in an elevated temperature environment such as gas turbine or combustion chambers.

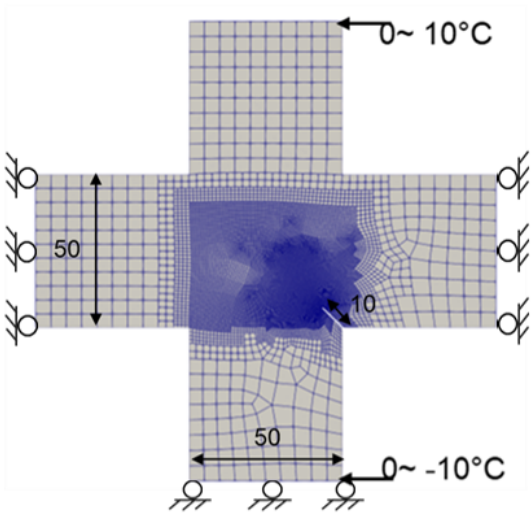

(a) Finite element mesh

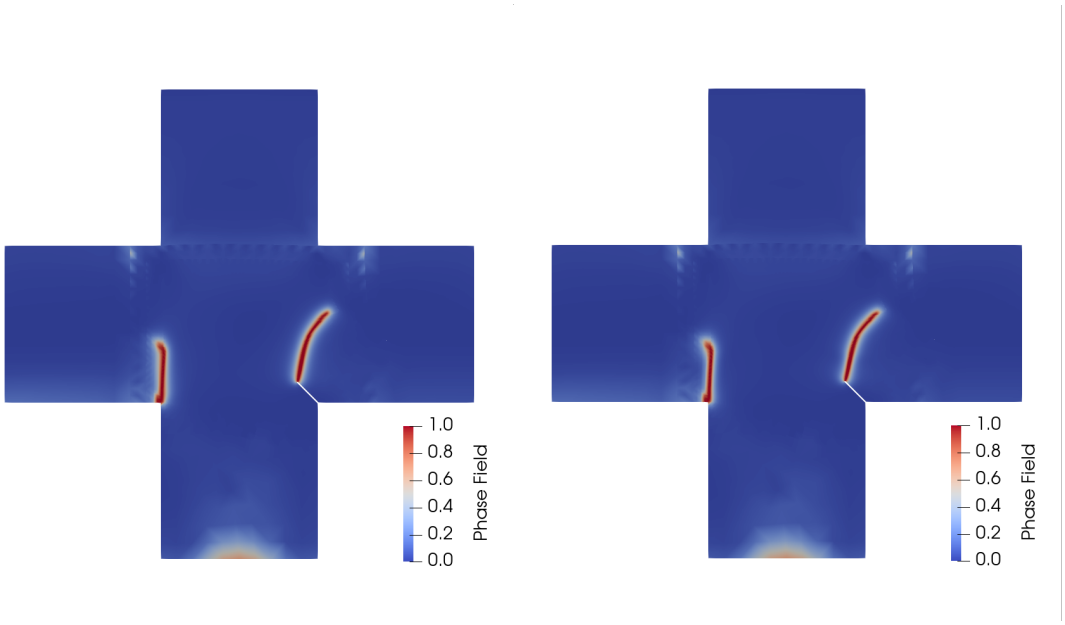

(b) Crack path by the first strategy

(c) Crack path by the second strategy

Figure 4.12: Crack propagation inside a cross-shaped sample under an imposed thermal gradient. At the top edge of the sample, the temperature is gradually increased from 0.0 ℃ to 10.0 ℃. At the bottom edge of the sample, the temperature is gradually decreased from 0.0 ℃ to -10.0 ℃. Two different solving strategies are applied to this coupled problem that involves the displacement field, the phase-field, and the temperature field.

The typical structure of a TBC system includes four layers [65], the top ceramic coat (TC), the thermal grown oxide (TGO), the metallic bond coat (BC), and the superalloy

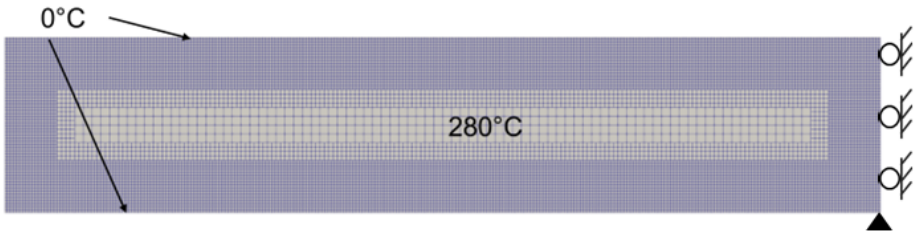

(a) Finite element mesh

(b) Temperature distribution

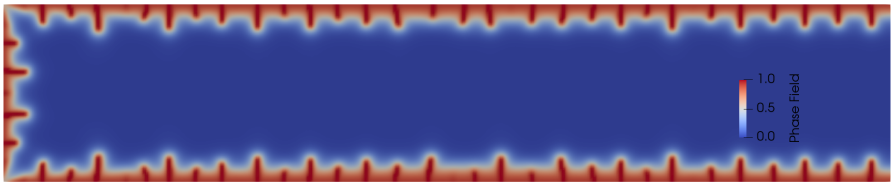

(c) Crack path distribution

Figure 4.13: A preheated sample is quenched in a 0 ℃ liquid. Due to the steep temperature gradient around the sample edges, multiple cracks are formed at the sample exterior and propagate into the sample interior, demonstrating the capability of the phase-field method in modeling complex crack patterns induced by the thermal effects.

substreate (SUB). Air plasma spraying (APS) and electron beam physical vapor deposition (EB-PVD) are two major processes used for TBC manufacturing [66, 67].

Cracks in TBCs can be generally classified as bulk cracks and interface cracks [68, 69]. However, the shapes of crack vary significantly due to different manufacturing processes [70, 71]. The main contributing factors causing the failure of TBCs include the mismatch among the thermal expansion coefficients of different layers, the swelling of the oxide between the top coat layer and the bound coat layer (also known as TGO growth), the

(a) Stress distribution at 10 ms

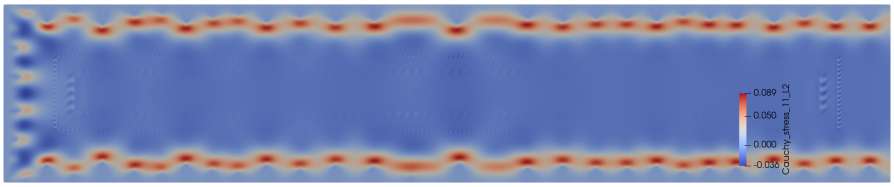

(b) Stress distribution at 50 ms

Figure 4.14: Normal stress σ_{11} (GPa) distribution during the quenching test: temperature gradient induces large stresses, causing the formation of cracks around the sample edges.

micro defects such as micro cracks and voids, and the complex microstructure of the interface between the TGO layer and the top coat layer [72].

Many numerical techniques have been developed in the past two decades to model the failure mechanism of the TBC system. Most of these models are based on the VCCT method or the XFEM [73, 74]. In recent years, the phase-field method becomes a popular choice in the research of the TBC failure mechanism [68, 75]. In this example, the phase-field approach is used to model the crack propagation inside a TBC system under the cooling effect. Figure 4.15 shows the TBC system used in this investigation [76], which is composed of a top layer with the thickness $H_4 = 100$ μm, a thermally grown oxide (TGO) layer with the thickness $H_3 = 6$ μm, a bond coat layer with the thickness $H_2 = 150$ μm, and a substrate layer with the thickness $H_1 = 1000$ μm. Particularly, the TGO layer is assumed to be sinusoidal with a wavelength $L = 30$ μm and an amplitude $A = 5$ μm. As a result, the TBC system is periodic along the x-direction. In order to effectively resolve the TGO layer that possesses the smallest thickness among all the components without significantly increasing the computational cost, we take advantage of the periodic structure of the TBC system by using a unit wavelength $L = 30$ μm as the computational domain. Meanwhile, the periodic boundary conditions are applied to the left and right edges, as

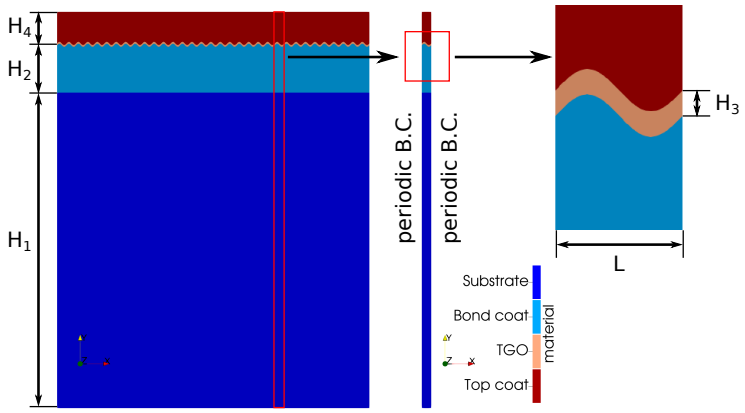

Figure 4.15: A typical TBC system has four layers with different thicknesses, including a top coat layer ($H_4 = 100$ μm) , a thermally grown oxide (TGO) layer ($H_3 = 6$ μm), a bond coat layer ($H_2 = 150$ μm), and a substrate layer ($H_1 = 1000$ μm). The TGO layer is assumed to have a sinusoidal shape with a wavelength $L = 30$ μm and an amplitude $A = 5$ μm. Due to the periodic structure, the computational domain only contains one sinusoidal period with the periodic boundary conditions applied on the left and right edges.

shown in Fig. 4.15. The material properties, including the mechanical properties and the thermal properties, of various TBC layers are listed in Tables 4.4 and 4.5. In this example, the TBC is uniformly cooled from 1000 ℃. Due to the mismatch of the thermal expansion coefficients between the TGO layer and the BC layer, cracks are initially formed at the interface between these two layers and further propagate, as shown in Figs 4.16b and 4.16c. Notice that in thees figures, even though the finite element simulation is performed across the entire thickness of the TBC system, only the region near the TGO and BC layers is shown for better visualization of the developed crack. This example demonstrates that the phase-field method can be used to model crack propagation in real-world engineering applications.

Table 4.4: Mechanical properties of various TBC layers used in the phase-field simulation.

Layer	Lamé λ (GPa)	Lamé μ (GPa)	critical energy release rate g_c (kN/mm)
TC	0.796	0.935	8×10^{-6}
TGO	96.6	122.95	50×10^{-6}
BC/TGO	126.92	84.62	10×10^{-6}
BC	126.92	84.62	300×10^{-6}

The normal stress distributions right before the crack formation and after crack formation are illustrated in Fig. 4.17a and 4.17b. The existence of crack significantly changes the stress distribution in different layers. In the current model, many assumptions are

Table 4.5: Thermal properties of various TBC layers used in the phase-field simulation.

Layer	CTE α (K^{-1})	conductivity κ ((W/(m· K))	heat capacity c (J/(kg· K))	density ρ (kg/m^3)
TC	11×10^{-6}	1.5	500	3.38×10^3
TGO	8×10^{-6}	25.0	880	3.95×10^3
BC/TGO	14×10^{-6}	4.3	501	7.32×10^3
BC	14×10^{-6}	4.3	501	7.32×10^3

made to simplify the simulation. At this stage, only thermal effect is considered as the dominant cause of TBC failure, i.e., only stresses induced by mismatch of the coefficient of thermal expansion (CTE) are the driving factor of crack propagation. In reality, the TGO growth, caused by the oxidation of material is another major reason of crack propagation in TBC system. The stress induced by oxidation effect is known as the growth stress. The fracture simulation combined with the TGO growth will be performed in future research.

4.3 Summary

In this chapter, the phase-field approach presented in Chapter 3 is used to model the crack propagation in several numerical examples. In the first set of examples, the crack is driven by the externally applied mechanical loads, such as tension, shear, and bending. In these examples, the staggered approach based on the alternate minimization and the monolithic approach based on the limited-memory BFGS method are adopted, which provide similar numerical results. It is shown that both solving strategies can effectively overcome the convergence difficulties arising from the non-convex energy functional of the phase-field crack formulation. Moreover, it is shown that the L-BFGS method requires fewer iterations to achieve convergence compared with the alternate minimization approach, making the former more appealing in large-scale finite element simulations. In the second set of examples, the crack is driven by the thermal effects. The phase-field crack approach can also successfully model the crack propagation process in the coupled multiphysics problem that involves the temperature field, the displacement field, the phase-field. Particularly, the phase-field crack approach is used to model the crack propagation in the thermal barrier coating system, demonstrating its potential to investigate failure mechanisms in real-world engineering applications.

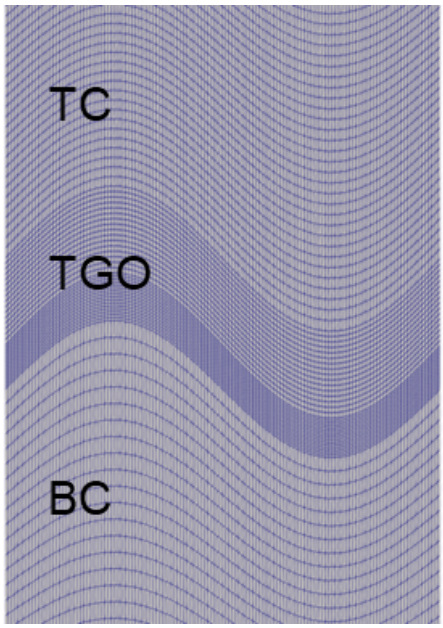

(a) Finite element mesh

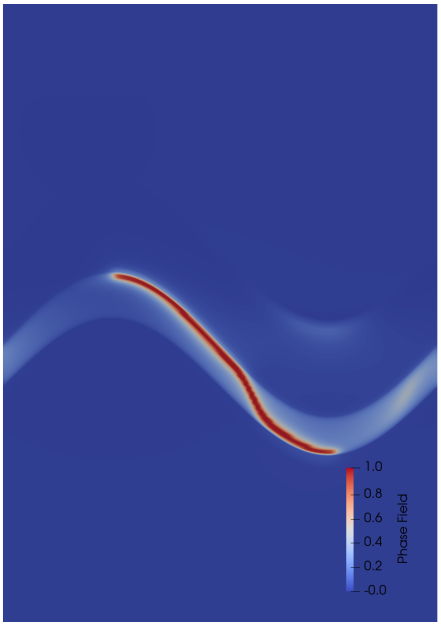

(b) Initial crack

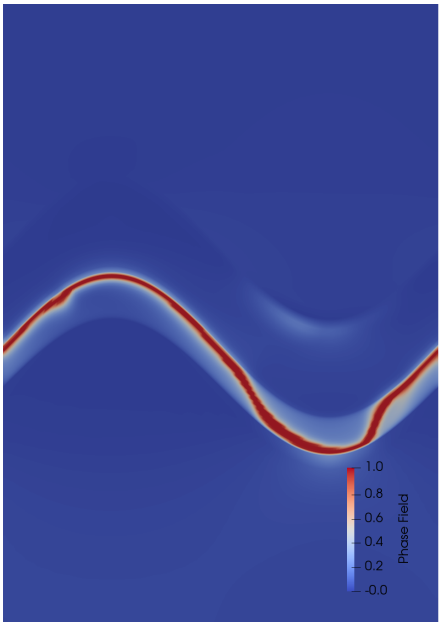

(c) Final crack

Figure 4.16: Phase-field simulation of the TBC system during a cooling stage. Due to the mismatch of the thermal expansion coefficient between the TGO layer and the BC layer, crack is initially formed at the interface between these two layers and further propagates.

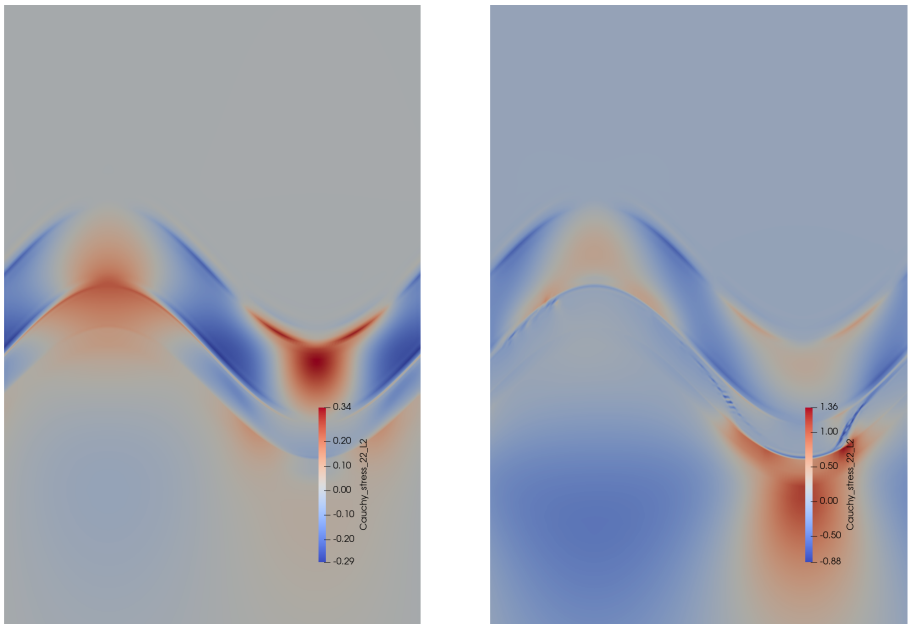

(a) Stress right before crack formation (b) Stress after final crack formation

Figure 4.17: Stress σ_{22} (GPa) distributions inside the TBC system during a cooling stage.

Chapter 5

Conclusions and future work

In this chapter, the major conclusions of this work are firstly summarized. Then, the limitation of the current work and potential avenues for future improvements are discussed.

5.1 Summary of the current work

Fracture mechanics is an important research topic in many engineering applications. Due to the difficulties associated with tracking complex crack patterns, previous computational methods such as the cohesive zone modeling and the extended finite element method only find limited successes in relatively simple crack propagation problems. The phase-field method becomes a popular choice in crack propagation modeling since this method can naturally handle complex crack geometries such as merging and branching. However, classical Newton-based nonlinear solving techniques typically face convergence difficulties caused by the non-convex energy functional of a fractured solid media. In this work, the following tasks are accomplished:

- The phase-field approach is combined with an adaptive mesh refinement technique to represent preexisting crack in a diffusive manner. The most prominent advantage of the phase-field approach to represent crack is that it is based on a variational structure, making this approach mathematically rigorous compared with other heuristic tracking strategies such as the level-set based method. However, the phase-field method is intrinsically expensive since highly refined meshes need to be used around the crack region. By combining the phase-field approach with the adaptive mesh refinement technique based on the so-called Kelly error estimator, the computational

cost could be significantly alleviated, making this method practical for real-world engineering problems.

- Various solving techniques are presented to robustly solve the coupled nonlinear system deduced from the phase-field crack approach, and their convergence performances are also compared. Due to the non-convexity of the total energy functional of the phase-field crack representation, conventional Newton-based approaches face convergence difficulties during nonlinear iterations. In order to overcome this difficulty, two solving approaches are presented in this work. The first approach is based on the alternate minimization, which belongs to the so-called staggered strategy and decomposes the coupled problem into two sub-problems such that the displacement field and the phase-field are updated separately. The second approach is based on the limited-memory BFGS method, which belongs to the so-called monolithic strategy and solves the displacement field and the phase-field simultaneously. Through several numerical examples, it is shown that both approaches could produce similar results. However, by comparing their convergence history, it is shown that in general the limited-memory BFGS approach requires fewer number of iterations in each load step, making this method more appealing for large-scale problems.

- The phase-field crack approach is further combined with a heat conduction problem to model crack propagation induced by thermal effects. In many engineering applications, such as the thermal barrier coating system, crack is not only caused by mechanical loads but also by thermal effects. Therefore, a heat conduction problem is combine with the phase-field crack approach to consider the impact of the temperature field on the crack propagation behavior. As a result, the problem includes three independent fields, the displacement field, the phase-field, and the temperature field. To robustly solve this three-field coupled problem, two solving approaches are presented. The first strategy follows the idea of the staggered strategy and fully decomposes the coupled problem into three sub-problems and update the temperature field, the displacement field, and the phase-field separately. The second strategy follows a mixed strategy, in which the temperature field is updated separately and the phase-field and the displacement field are updated simultaneously using the limited-memory BFGS approach. Both solving approaches can properly model the thermal-induced crack propagation, though the second approach is more advantageous since it requires fewer number of iterations to update the displacement field and the phase-field.

The original contributions of this thesis include:

- Extended the limited-memory BFGS (L-BFGS) method, originally proposed by Prof. Tao Jin's group [34], from the mechanical phase-field problem to the thermomechanically coupled phase-field problem.
- Demonstrated the equivalence of the staggered approach and the L-BFGS monolithic approach in the phase-field formulation. Moreover, the latter requires fewer iterations to achieve convergence during the nonlinear solving process.
- Implemented the computational framework in the deal.II library [48], which can be extended to solve more complex problems in the future.

Besides the above contributions, all the presented numerical algorithms and examples are implemented in deal.II [48], which is an open-source C++ finite element library. All the source codes and input files used in this thesis can be found on GitHub[1].

5.2 Future work

The current work has several limitations and can be potentially further improved via several avenues:

- Generally speaking, the monolithic approach is more appealing compared with the staggered approach since it requires fewer number of nonlinear iterations to achieve convergence than the latter. For the thermal-induced crack propagation problem, only a fully staggered approach and a mixed approach are presented, and the fully monolithic approach is yet to be developed. The difficulty comes from the fact that it is still unclear how to introduce the thermal effect into the total energy functional, which is required by the limited-memory BFGS approach. One of the future directions is to develop the fully monolithic approach that solves for the temperature field, the displacement field, and the phase-field simultaneously, which could significantly reduce the wall clock time required by the thermal-induced phase-field crack propagation problem.
- During the crack modeling of the thermal barrier coating (TBC), cracks are solely driven by the mismatch of the thermal expansion coefficients among various TBC layers. In reality, the failure mechanisms of the TBC system is much more complex. For instance, it is reported that the oxidation is also an important process to drive

[1] https://github.com/taojinllnl/

crack growth [68, 72]. In order to consider the oxidation impact, a reaction-diffusion model [77] can be further combined with the phase-field crack approach. However, this approach will inevitably make the solving process of the coupled system even more challenging.

Table 5.1: Material properties of a fiber-reinforced composite material.

Parameter	Value
Fiber Young's modulus	40.0 GPa
Fiber Poisson's ratio	0.33
Matrix Young's modulus	4.0 GPa
Matrix critical energy release rate	0.25 N/mm
Interface critical energy release rate	0.05 N/mm

- Currently, the interfaces among various material components in a complex engineering system such as TBC are not directly considered. As a result, the material properties change significantly at the boundary shared by two different components, which might deviate from the physical reality. One approach is to use the so-called diffusive interface model [78, 79], which could more accurately consider the interfaces between different material components. This is particularly relevant for the modeling of the TBC system.

- The phase-field method can be used to investigate crack propagation in other complex engineering materials such as composites. For instance, Fig. 5.1 shows an example of using the phase-field method to model crack propagation inside a composite material. The material parameters for the fiber and the surrounding matrix are listed in Table 5.1.

- The phase-field method can be combined with fatigue failure model [80]. In response to fatigue effect, an extended degradation function is needed to evaluate the reduction of fracture toughness due to accumulated damage induced by cycling load. Eq. (5.1) is one typical fatigue degradation function [81, 82]

$$f(\beta) = \begin{cases} 1 \\ (\frac{2\beta_T}{\beta+\beta_T})^2 \end{cases} \tag{5.1}$$

where $\beta = \beta(t)$ is a cumulative history variable and β_T is the fatigue threshold of material. The corresponding phase-field equation in Eq. (3.19a) is then modified

as [81, 82]

$$g'(d)\mathcal{H} + \frac{g_c}{l}(f(\beta)d - l^2\nabla(\nabla f(\beta)d)) = 0 \tag{5.2}$$

Detailed numerical implementation can be found in [80–82].

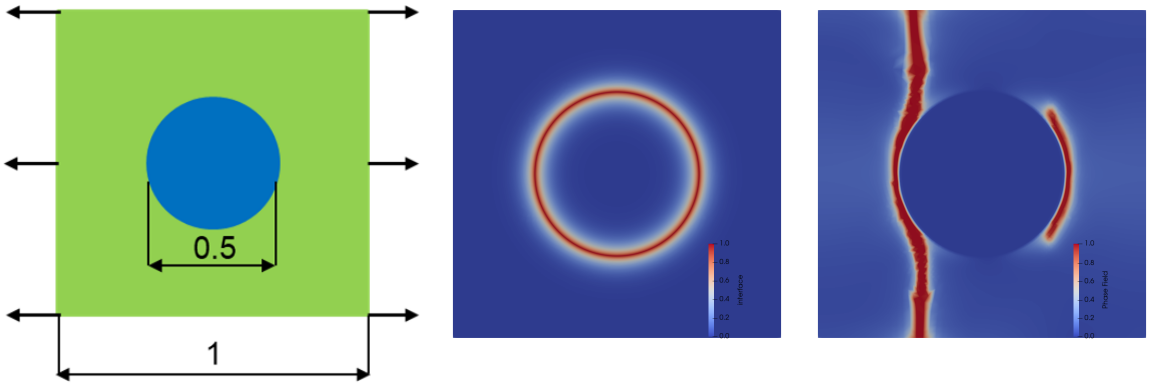

(a) Unit cell (b) Diffusive interface (c) Crack propagation

Figure 5.1: Crack propagation modeled by the phase-field approach inside an unit cell of the fiber-reinforced composite: (a) unit cell of a fiber-reinforced composite material, (b) diffusive interface at the fiber-matrix, and (c) crack propagation in the composite material. The interface between the fiber and the surrounding matrix is modeled by the diffusive interface technique.

- As discussed in Chapter 3, the L-BFGS method uses vector pairs to update matrix, thus, it is compatible with parallel computing to take advantage of modern computer architecture. In order to model 3D crack propagation in large-scale simulations, parallel computing via MPI (Message Passing Interface) [83] can be involved in future research.

References

[1] Wikipedia contributors. Fracture mechanics — Wikipedia, the free encyclopedia, 2024. [Online; accessed 15-February-2025].

[2] Ronald Krueger. Virtual crack closure technique: History, approach, and applications. *Appl. Mech. Rev.*, 57(2):109–143, 2004.

[3] AS Vagbharathi and S Gopalakrishnan. An extended finite-element model coupled with level set method for analysis of growth of corrosion pits in metallic structures. *Proceedings of the Royal Society A: Mathematical, Physical and Engineering Sciences*, 470(2168):20140001, 2014.

[4] Thanh Tung Nguyen, Julien Yvonnet, Q-Z Zhu, Michel Bornert, and Camille Chateau. A phase field method to simulate crack nucleation and propagation in strongly heterogeneous materials from direct imaging of their microstructure. *Engineering Fracture Mechanics*, 139:18–39, 2015.

[5] F. Armero and J. Kim. Three-dimensional finite elements with embedded strong discontinuities to model material failure in the infinitesimal range. *International Journal for Numerical Methods in Engineering*, 91(12):1291–1330, 2012.

[6] Tao Jin, Hashem M. Mourad, and Curt A. Bronkhorst. A comparative study of shear band tracking strategies in three-dimensional finite elements with embedded weak discontinuities. *Finite Elements in Analysis and Design*, 155:11–31, 2019.

[7] Tao Jin, Hashem M. Mourad, Curt A. Bronkhorst, Veronica Livescu, Xiaoxuan Zhang, Christian Linder, and Richard A. Regueiro. Three-dimensional explicit finite element formulation for shear localization with global tracking of embedded weak discontinuities. *Computer Methods in Applied Mechanics and Engineering*, 353:416–447, 2019.

[8] Ted L Anderson and Ted L Anderson. *Fracture mechanics: fundamentals and applications*. CRC press, 2005.

[9] L.B. Freund and L.B. Freud. *Dynamic Fracture Mechanics*. Cambridge Monographs on Mechanics. Cambridge University Press, 1998.

[10] Alan Arnold Griffith. Vi. the phenomena of rupture and flow in solids. *Philosophical transactions of the royal society of london. Series A, containing papers of a mathematical or physical character*, 221(582-593):163–198, 1921.

[11] FA McClintock and GR Irwin. *Plasticity aspects of fracture mechanics*. ASTM International West Conshohocken, 1965.

[12] Nicolas Moës, John Dolbow, and Ted Belytschko. A finite element method for crack growth without remeshing. *International journal for numerical methods in engineering*, 46(1):131–150, 1999.

[13] Ted Belytschko and Tom Black. Elastic crack growth in finite elements with minimal remeshing. *International journal for numerical methods in engineering*, 45(5):601–620, 1999.

[14] M Cervera, GB Barbat, Michele Chiumenti, and J-Y Wu. A comparative review of xfem, mixed fem and phase-field models for quasi-brittle cracking. *Archives of Computational Methods in Engineering*, 29(2):1009–1083, 2022.

[15] Bořek Patzák and Milan Jirásek. Process zone resolution by extended finite elements. *Engineering Fracture Mechanics*, 70(7-8):957–977, 2003.

[16] Thomas Carraro and Sven Wetterauer. On the implementation of the extended finite element method (xfem) for interface problems. *arXiv preprint arXiv:1507.04238*, 2015.

[17] Stanley Osher and Ronald P Fedkiw. Level set methods: an overview and some recent results. *Journal of Computational physics*, 169(2):463–502, 2001.

[18] Natarajan Sukumar, Nicolas Moës, Brian Moran, and Ted Belytschko. Extended finite element method for three-dimensional crack modelling. *International journal for numerical methods in engineering*, 48(11):1549–1570, 2000.

[19] Marc Duflot. The extended finite element method in thermoelastic fracture mechanics. *International Journal for Numerical Methods in Engineering*, 74(5):827–847, 2008.

[20] René De Borst. Numerical aspects of cohesive-zone models. *Engineering fracture mechanics*, 70(14):1743–1757, 2003.

[21] Donald S Dugdale. Yielding of steel sheets containing slits. *Journal of the Mechanics and Physics of Solids*, 8(2):100–104, 1960.

[22] Grigory I Barenblatt. The formation of equilibrium cracks during brittle fracture. general ideas and hypotheses. axially-symmetric cracks. *Journal of applied mathematics and mechanics*, 23(3):622–636, 1959.

[23] Michael Ortiz and Anna Pandolfi. Finite-deformation irreversible cohesive elements for three-dimensional crack-propagation analysis. *International journal for numerical methods in engineering*, 44(9):1267–1282, 1999.

[24] Christian Miehe, Martina Hofacker, and Fabian Welschinger. A phase field model for rate-independent crack propagation: Robust algorithmic implementation based on operator splits. *Computer Methods in Applied Mechanics and Engineering*, 199(45-48):2765–2778, 2010.

[25] Christian Miehe, Fabian Welschinger, and Martina Hofacker. Thermodynamically consistent phase-field models of fracture: Variational principles and multi-field fe implementations. *International journal for numerical methods in engineering*, 83(10):1273–1311, 2010.

[26] Marreddy Ambati, Tymofiy Gerasimov, and Laura De Lorenzis. A review on phase-field models of brittle fracture and a new fast hybrid formulation. *Computational Mechanics*, 55(2):383–405, 2015.

[27] Timo Heister, Mary F. Wheeler, and Thomas Wick. A primal-dual active set method and predictor-corrector mesh adaptivity for computing fracture propagation using a phase-field approach. *Computer Methods in Applied Mechanics and Engineering*, 290:466–495, 2015.

[28] Jian-Ying Wu. A unified phase-field theory for the mechanics of damage and quasi-brittle failure. *Journal of the Mechanics and Physics of Solids*, 103:72–99, 2017.

[29] Thomas Wick. Modified newton methods for solving fully monolithic phase-field quasi-static brittle fracture propagation. *Computer Methods in Applied Mechanics and Engineering*, 325:577–611, 2017.

[30] Emilio Martinez-Pañeda, Alireza Golahmar, and Christian F. Niordson. A phase field formulation for hydrogen assisted cracking. *Computer Methods in Applied Mechanics and Engineering*, 342:742–761, 2018.

[31] Jian-Ying Wu, Yuli Huang, and Vinh Phu Nguyen. On the BFGS monolithic algorithm for the unified phase field damage theory. *Computer Methods in Applied Mechanics and Engineering*, 360:112704, 2020.

[32] Lampros Svolos, Curt A. Bronkhorst, and Haim Waisman. Thermal-conductivity degradation across cracks in coupled thermo-mechanical systems modeled by the phase-field fracture method. *Journal of the Mechanics and Physics of Solids*, 137:103861, 2020.

[33] Andre Costa, Matteo Cusini, Tao Jin, Randolph Settgast, and John E. Dolbow. A multi-resolution approach to hydraulic fracture simulation. *International Journal of Fracture*, 237(1):165–188, 2022.

[34] Tao Jin, Zhao Li, and Kuiying Chen. A novel phase-field monolithic scheme for brittle crack propagation based on the limited-memory bfgs method with adaptive mesh refinement. *International Journal for Numerical Methods in Engineering*, page e7572, 2024.

[35] Tao Jin. Gradient projection method for enforcing crack irreversibility as box constraints in a robust monolithic phase-field scheme. *Computer Methods in Applied Mechanics and Engineering*, 435:117622, 2025.

[36] Gilles A Francfort and J-J Marigo. Revisiting brittle fracture as an energy minimization problem. *Journal of the Mechanics and Physics of Solids*, 46(8):1319–1342, 1998.

[37] Blaise Bourdin, Gilles A Francfort, and Jean-Jacques Marigo. Numerical experiments in revisited brittle fracture. *Journal of the Mechanics and Physics of Solids*, 48(4):797–826, 2000.

[38] Blaise Bourdin, Gilles A Francfort, and Jean-Jacques Marigo. The variational approach to fracture. *Journal of elasticity*, 91:5–148, 2008.

[39] M.F. Wheeler, T. Wick, and W. Wollner. An augmented-lagrangian method for the phase-field approach for pressurized fractures. *Computer Methods in Applied Mechanics and Engineering*, 271:69–85, 2014.

[40] J. Wambacq, J. Ulloa, G. Lombaert, and S. François. Interior-point methods for the phase-field approach to brittle and ductile fracture. *Computer Methods in Applied Mechanics and Engineering*, 375:113612, 2021.

[41] Bruno A Boley and Jerome H Weiner. *Theory of thermal stresses*. Courier Corporation, 2012.

[42] Carlos A Felippa, Kwang-Chun Park, and Charbel Farhat. Partitioned analysis of coupled mechanical systems. *Computer methods in applied mechanics and engineering*, 190(24-25):3247–3270, 2001.

[43] Yingfeng Shao, Yue Zhang, Xianghong Xu, Zhiliang Zhou, Wei Li, and Boyang Liu. Effect of crack pattern on the residual strength of ceramics after quenching. *Journal of the American Ceramic Society*, 94(9):2804–2807, 2011.

[44] YF Fu, YL Wong, CA Tang, and Chi Sun Poon. Thermal induced stress and associated cracking in cement-based composite at elevated temperatures—-part i: Thermal cracking around single inclusion. *Cement and Concrete Composites*, 26(2):99–111, 2004.

[45] SB Tang, H Zhang, CA Tang, and HY Liu. Numerical model for the cracking behavior of heterogeneous brittle solids subjected to thermal shock. *International Journal of Solids and Structures*, 80:520–531, 2016.

[46] I Özdemir, WAM Brekelmans, and MGD05797160 Geers. A thermo-mechanical cohesive zone model. *Computational Mechanics*, 46:735–745, 2010.

[47] Thomas Menouillard and Ted Belytschko. Analysis and computations of oscillating crack propagation in a heated strip. *International journal of fracture*, 167:57–70, 2011.

[48] Daniel Arndt, Wolfgang Bangerth, Marco Feder, Marc Fehling, Rene Gassmöller, Timo Heister, Luca Heltai, Martin Kronbichler, Matthias Maier, Peter Munch, Jean-Paul Pelteret, Simon Sticko, Bruno Turcksin, and David Wells. The `deal.II` library, version 9.4. *Journal of Numerical Mathematics*, 30(3):231–246, 2022.

[49] D. W. Kelly, J. P. De S. R. Gago, O. C. Zienkiewicz, and I. Babuska. A posteriori error analysis and adaptive processes in the finite element method: Part i - error analysis. *International Journal for Numerical Methods in Engineering*, 19(11):1593–1619, 1983.

[50] Mark S. Shephard. Linear multipoint constraints applied via transformation as part of a direct stiffness assembly process. *International Journal for Numerical Methods in Engineering*, 20(11):2107–2112, 1984.

[51] Jian-Ying Wu, Yuli Huang, and Vinh Phu Nguyen. On the bfgs monolithic algorithm for the unified phase field damage theory. *Computer Methods in Applied Mechanics and Engineering*, 360:112704, 2020.

[52] C. Miehe. Comparison of two algorithms for the computation of fourth-order isotropic tensor functions. *Computers & Structures*, 66(1):37–43, 1998.

[53] Christian Miehe and Matthias Lambrecht. Algorithms for computation of stresses and elasticity moduli in terms of seth–hill's family of generalized strain tensors. *Communications in Numerical Methods in Engineering*, 17(5):337–353, 2001.

[54] Christian Miehe. Comparison of two algorithms for the computation of fourth-order isotropic tensor functions. *Computers & structures*, 66(1):37–43, 1998.

[55] Christian Miehe and Matthias Lambrecht. Algorithms for computation of stresses and elasticity moduli in terms of seth–hill's family of generalized strain tensors. *Communications in numerical methods in engineering*, 17(5):337–353, 2001.

[56] William C Davidon. Variable metric method for minimization. *SIAM Journal on optimization*, 1(1):1–17, 1991.

[57] Jorge Nocedal. Updating quasi-newton matrices with limited storage. *Mathematics of computation*, 35(151):773–782, 1980.

[58] Jorge Nocedal and Stephen J. Wright. *Numerical optimization (2nd edition)*. Springer New York, NY, 2006.

[59] Tushar Kanti Mandal, Vinh Phu Nguyen, Jian-Ying Wu, Chi Nguyen-Thanh, and Alban de Vaucorbeil. Fracture of thermo-elastic solids: Phase-field modeling and new results with an efficient monolithic solver. *Computer Methods in Applied Mechanics and Engineering*, 376:113648, 2021.

[60] Tiancheng Zhang, Tinh Quoc Bui, Tiantang Yu, Yicong Li, and Sundararajan Natarajan. Quasi-static thermoelastic fracture: Adaptive phase-field modeling with variable-node elements. *Theoretical and Applied Fracture Mechanics*, 124:103811, 2023.

[61] Jean Salençon. *Handbook of continuum mechanics: General concepts thermoelasticity*. Springer Science & Business Media, 2012.

[62] Tymofiy Gerasimov and Laura De Lorenzis. A line search assisted monolithic approach for phase-field computing of brittle fracture. *Computer Methods in Applied Mechanics and Engineering*, 312:276–303, 2016.

[63] Nitin P Padture, Maurice Gell, and Eric H Jordan. Thermal barrier coatings for gas-turbine engine applications. *Science*, 296(5566):280–284, 2002.

[64] AG Evans, MY He, and JW Hutchinson. Mechanics-based scaling laws for the durability of thermal barrier coatings. *Progress in materials science*, 46(3-4):249–271, 2001.

[65] YQ Xiao, L Yang, W Zhu, YC Zhou, ZP Pi, and YG Wei. Delamination mechanism of thermal barrier coatings induced by thermal cycling and growth stresses. *Engineering Failure Analysis*, 121:105202, 2021.

[66] Benjamin Bernard, Aurélie Quet, Luc Bianchi, Aurélien Joulia, André Malié, Vincent Schick, and Benjamin Rémy. Thermal insulation properties of ysz coatings: suspension plasma spraying (sps) versus electron beam physical vapor deposition (eb-pvd) and atmospheric plasma spraying (aps). *Surface and Coatings Technology*, 318:122–128, 2017.

[67] H-J Rätzer-Scheibe and Uwe Schulz. The effects of heat treatment and gas atmosphere on the thermal conductivity of aps and eb-pvd pysz thermal barrier coatings. *Surface and Coatings Technology*, 201(18):7880–7888, 2007.

[68] QQ Zhou, L Yang, C Luo, FW Chen, YC Zhou, and YG Wei. Thermal barrier coatings failure mechanism during the interfacial oxidation process under the interaction between interface by cohesive zone model and brittle fracture by phase-field. *International Journal of Solids and Structures*, 214:18–34, 2021.

[69] L Wang, JS Yang, JX Ni, CG Liu, XH Zhong, F Shao, HY Zhao, SY Tao, and Y Wang. Influence of cracks in aps-tbcs on stress around tgo during thermal cycling: A numerical simulation study. *Surface and Coatings Technology*, 285:98–112, 2016.

[70] H Echsler, V Shemet, M Schütze, L Singheiser, and WJ Quadakkers. Cracking in and around the thermally grown oxide in thermal barrier coatings: A comparison of isothermal and cyclic oxidation. *Journal of Materials science*, 41:1047–1058, 2006.

[71] Duoqi Shi, Jianan Song, Shaolin Li, Hongyu Qi, and Xiaoguang Yang. Cracking behaviors of eb-pvd thermal barrier coating under temperature gradient. *Ceramics International*, 45(15):18518–18528, 2019.

[72] Lang Min, Zilong Wang, Xiaofei Hu, Dan Zhao, Zhi Sun, Peng Zhang, Weian Yao, and Tinh Quoc Bui. A chemo-thermo-mechanical coupled phase field framework for

failure in thermal barrier coatings. *Computer Methods in Applied Mechanics and Engineering*, 411:116044, 2023.

[73] L Wang, DC Li, JS Yang, F Shao, XH Zhong, HY Zhao, K Yang, SY Tao, and Y Wang. Modeling of thermal properties and failure of thermal barrier coatings with the use of finite element methods: A review. *Journal of the European Ceramic Society*, 36(6):1313–1331, 2016.

[74] Zhi-Yuan Wei, Hong-Neng Cai, and Chang-Jiu Li. Comprehensive dynamic failure mechanism of thermal barrier coatings based on a novel crack propagation and tgo growth coupling model. *Ceramics International*, 44(18):22556–22566, 2018.

[75] YQ Xiao, ZY Liu, XM Peng, W Zhu, YC Zhou, and L Yang. Spallation mechanism of thermal barrier coatings with real interface morphology considering growth and thermal stresses based on fracture phase field. *Surface and Coatings Technology*, 458:129356, 2023.

[76] Zhao Li, Kuiying Chen, and Tao Jin. Finite element simulations of the thermomechanically coupled responses of thermal barrier coating systems using an unconditionally stable staggered approach. *Applied Mathematical Modelling*, 138:115750, 2025.

[77] TS Hille, S Turteltaub, and ASJ Suiker. Oxide growth and damage evolution in thermal barrier coatings. *Engineering Fracture Mechanics*, 78(10):2139–2152, 2011.

[78] Peng Zhang, Xiaofei Hu, Shangtong Yang, and Weian Yao. Modelling progressive failure in multi-phase materials using a phase field method. *Engineering Fracture Mechanics*, 209:105–124, 2019.

[79] Xiaofei Hu, Peng Zhang, and Weian Yao. Phase field modelling of microscopic failure in composite laminates. *Journal of Composite Materials*, 55(14):1853–1865, 2021.

[80] Peidong Li, Weidong Li, Biao Li, Shuo Yang, Yongxing Shen, Qingyuan Wang, and Kun Zhou. A review on phase field models for fracture and fatigue. *Engineering Fracture Mechanics*, 289:109419, 2023.

[81] Pietro Carrara, Marreddy Ambati, Roberto Alessi, and Laura De Lorenzis. A framework to model the fatigue behavior of brittle materials based on a variational phase-field approach. *Computer Methods in Applied Mechanics and Engineering*, 361:112731, 2020.

[82] Junlei Ding, Tiantang Yu, Weihua Fang, and Sundararajan Natarajan. An adaptive phase field modeling of fatigue crack growth using variable-node elements and explicit cycle jump scheme. *Computer Methods in Applied Mechanics and Engineering*, 429:117200, 2024.

[83] William Gropp, Ewing Lusk, and Anthony Skjellum. *Using MPI: portable parallel programming with the message-passing interface*, volume 1. MIT press, 1999.